View metadata, citation and similar papers at core.ac.uk

brought to you by CORE

provided by NASA Technical Reports Server

National Aeronautics and Space Administration

PD-B-78-175

George C. Marshall Space Flight Center
Marshall Space Flight Center Alabama 35812

PLUME RF INTERFERENCE CALCULATIONS FOR SPACE SHUTTLE

BY

FREDERICK P. BOYNTON
P.S. RAJASEKHAR
PHYSICAL DYNAMICS, INC.
P.O. Box 1069
BERKELEY, CALIFORNIA 94701

(NASA-CR-161099) PLUME RF INTERFERENCE CALCULATIONS FOR SPACE SHUTTLE Final Report (Physical Dynamics, Inc., Berkeley, Calif.) 64 p HC A04/MF A01 CSCL 20H

N79-17900

Unclas
G3/16 14145

RECEIVED NASA STI FACILITY ACCESS DEPT

FINAL REPORT ON ADDED TASKS
CONTRACT No. NAS8-32528

PREPARED FOR

GEORGE C. MARSHALL SPACE FLIGHT CENTER
MARSHALL SPACE FLIGHT CENTER, ALABAMA

MAY 1978

TABLE OF CONTENTS

1.0 INTRODUCTION

Concern exists that the large and relatively highly ionized exhaust plumes of the Space Shuttle's solid rocket motors (SRM's) may impede communication with the vehicle under some conditions. In particular, the vehicle's ability to receive arming and destruct commands from a ground-based Range Safety system under conditions where the exhaust plume intercepts the line of sight has been questioned.

Under a previous contract with the George C. Marshall Space Flight Center, Physical Dynamics, Inc., performed theoretical calculations of signal attenuation by the exhaust plumes of both the Space Shuttle and the Titan III-C. These studies (Boynton, et al., 1977a) indicated that a large attenuation, 30-80 db, could be expected under some conditions. Subsequent studies (Boynton, et al., 1977b) showed that the calculated attenuation levels could result in marginally acceptable power levels for the signal reaching the Shuttle for combinations of northerly launch azimuth, high altitude, and nominal (Cape site) transmitter location. This work is reviewed in Section 2.

During a static ground test of a full-scale SRM at Thiokol, Utah, measurements of attenuation of the UHF 416.5 MHz Range Safety Signal, the VHF voice link (230 MHz) and of S-band (c. 2.2 GHz) communications links were undertaken. These measurements were sponsored by the Johnson Space Center and conducted by the Goddard Space Flight Center. Analyses of these results by Kalil (1977) indicated that measurable attenuation did occur at all tested frequencies. The measured attenuation levels were compared with a simple model proposed by Vicente, et al. (1967), in which the received signal is identified as that diffracted about the edge of the highly absorbing plume and the signal level in the shadow zone is evaluated using the formula for diffraction at a straight-edge. The comparison was satisfactory at VHF and UHF frequencies, and slightly less so at S-band.

The ground test attenuation measurements offer a further opportunity to compare our computations with experimental data. (Comparisons with in-flight measurements were presented in our earlier report.) We have found excellent agreement between the results of experiment and on calculations at the Range Safety signal frequency of 416.5 MHz. At S-band the agreement is not good; possible reasons for the discrepancies at the higher frequency are discussed in Section 4.

In testing a revised version of the computer code (FRENL) which incorporates our techniques, we discovered a numerical error which had not appeared in previous exercises of the procedure. The error causes the calculation to underestimate the signal strength in the deeply shadowed zone. Tests of our technique for a diffraction problem which has an analytic solution (see Section 3) led to development of a criterion for accuracy of the computation. Our ground test calculations satisfy the accuracy criterion; the in-flight calculations performed earlier do not.

A revised procedure which appears to relieve the accuracy problem with the original procedure has been developed; this procedure is discussed in Section 5. Applications of the revised procedure to high-altitude SRM plume attenuation are presented in Section 6.

2.0 REVIEW OF PREVIOUS WORK

The SRM exhaust plume is a weakly ionized plasma which attenuates and refracts electromagnetic waves incident upon it. The propagation geometry usually involves relatively small-angle scattering of the incident radiation, and so it is appropriate to apply a paraxial (parabolic wave) treatment. Accurate and efficient procedures for evaluating solutions to the parabolic wave equation have been developed for other applications, including radio wave propagation in the ionosphere, laser beam propagation in the atmosphere, and acoustic wave propagation in the ocean. These procedures are classified as split operator techniques, in which a dielectric medium is modelled as a sequence of phase screens which produce attenuation and phase shifts of waves incident upon them. Propagation between these phase screens is treated in terms of the Fresnel-Kirchhoff integral, and fast Fourier transforms (FFT's) are used to evaluate the convolution over a plane on which the complex wave amplitude ψ is prescribed.

In plume attenuation calculations, the propagation was treated as if it occurred from the vehicle-mounted antenna to a ground-based receiver, rather than from a ground-based transmitter to the vehicle. A well-known reciprocity principle equates the signal amplitude transmitted along any given path to that transmitted in the opposite direction along the same path; in our calculations, all reasonable paths between a transmitter and receiver are included. The calculation in the "reverse" direction is convenient for examining the effects of ground site location, since a large number of ground points are included. Problems introduced by ray divergence when considering propagation from the antenna are dealt with by introducing a geometric transformation due originally to Talanov (1970), which converts a nearly spherical wave front to a nearly plane wave front by subtracting a phase correction and correspondingly introduces an altered propagation distance. Thus rezoning to avoid aliasing in the FFT operations is eliminated.

The sequence of calculations is thus as follows:

1) Prescribe the complex wave field amplitude $\psi_{Z_o}(x', y')$ at some initial plane Z_o where the plume is not present.
2) Apply the Talanov transformation to remove divergence effects in $\psi_{Z_o}(x', y')$.
3) Perform a free-space propagation calculation between the planes Z_o and Z_1, Z_1 containing the first phase screen representing the plume. The following steps are carried out:
   a) Evaluate the discrete Fourier transform of ψ_{Z_o} by FFT procedures.
   b) Multiply the result, $\hat{\psi}_{Z_o}(k_x, k_y)$ by $\exp\{-i\,\Delta Z'(k_x^2 + k_y^2)/2k_o\}$, the transform of the propagation kernel in the Fresnel approximation. Here k_o is the nominal propagation wavenumber and $\Delta Z'$ is the effective plane-wave propagation distance given by $\Delta Z' = (Z_1 - Z_o)\, Z_f/[(Z_1 - Z_o) + Z_f]$, with Z_f the distance from Z_o to the antenna (considered as a point source). The result of this step is the discrete Fourier transform of the wave amplitude incident upon the plane Z_1, $\hat{\psi}'_{Z_1}(k_x, k_y)$.
   c) Take the inverse Fourier transform of $\hat{\psi}_{Z_1}$ to give the amplitude in physical space.
4) Apply an inverse Talanov transformation to reconvert the plane wave to the actual spherical wave. Adjust the mesh size and the modulus of the wave amplitude by the appropriate geometric factors.
5) Introduce a complex phase shift due to the phase screen representing the plume as follows:

a) Evaluate the local complex refractive index of the plume based upon local values of the electron density and collision frequency.

b) Calculate the complex phase shift through a phase screen of thickness $\Delta Z = \frac{1}{2}(Z_2 - Z_0)$. Here $\phi + i\alpha = k_0(n-1)\Delta Z$, where n is the index of refraction.

c) Multiply $\psi'_{Z_1}(x,y)$ by $\exp(i\phi - \alpha)$ to give the wave amplitude emerging from the phase screen at Z_1, $\psi_{Z_1}(x,y)$.

6) Cycle through steps 2-5 for the successive planes $Z_2, Z_3, \cdots Z_n$ until the entire plume has been traversed.

7) Perform a final propagation calculation (steps 2-4) to a distant plane in the vicinity of the ground station. Provided that this plane is sufficiently distant, further propagation should not change the properties of the field amplitude when expressed as a function of angle with respect to a nominal propagation direction (usually tail aspect).

Figure 1 shows the propagation calculation in schematic form; Figure 2 shows the effects of the Talanov transformation (focusing/defocusing).

Properties of the exhaust plumes of Titan III-C and Space Shuttle SRM's at selected altitudes were furnished to us by Lockheed Missiles and Space Company (Huntsville Research and Engineering Center). The results of attenuation calculations for the Titan III-C at VHF and S-band frequencies were compared with field data presented by Poehler (1969); our calculations were somewhat conservative (low) with respect to the observed signal power levels at VHF (Figure 3), and significantly conservative at S-band (Figure 4. Results for the Space Shuttle at high altitude (37.5 km) indicated that high attenuation could be expected near tail aspects (Figure 5). When combined with trajectory data and ground site configuration, these

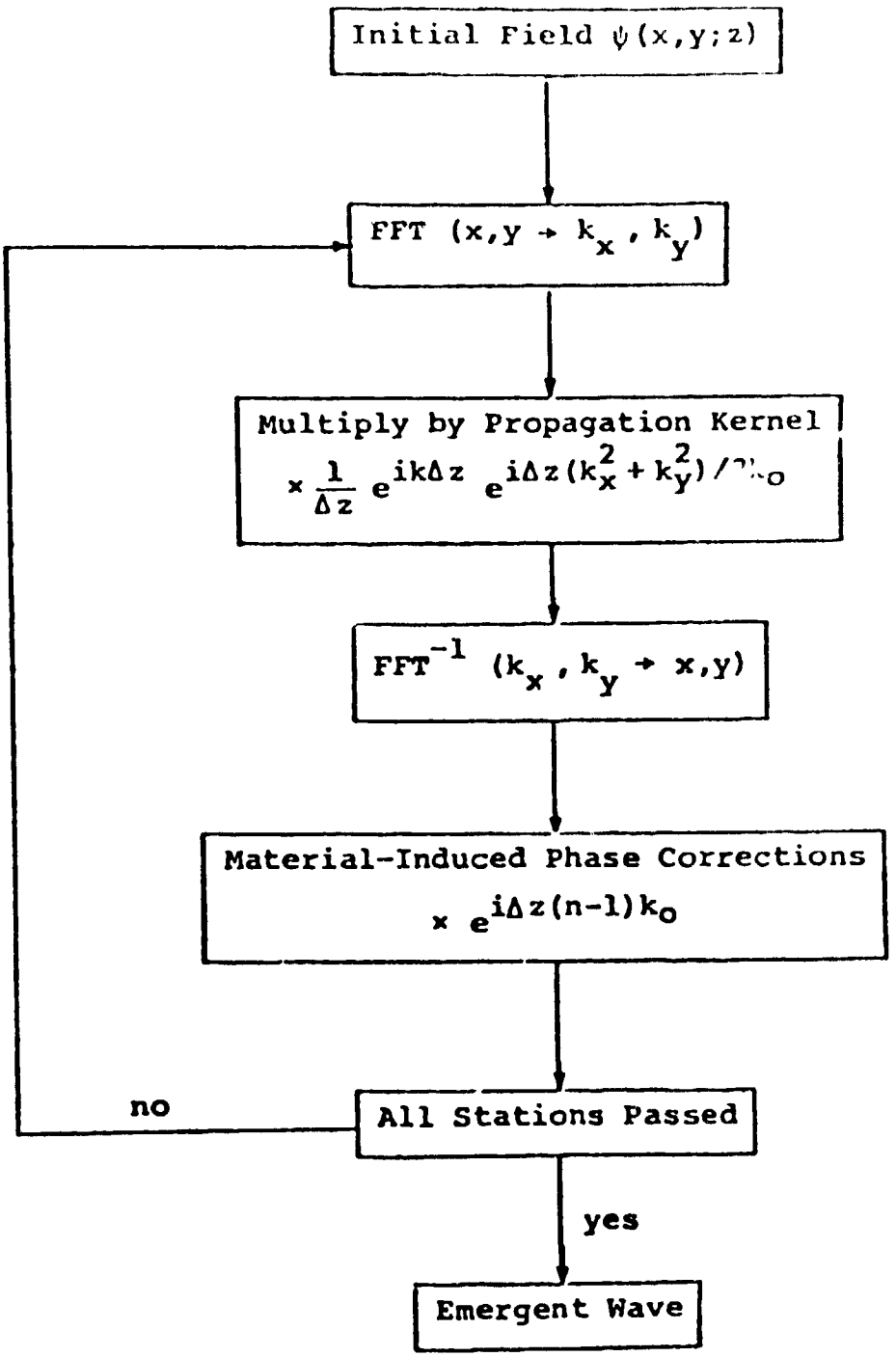

Figure 1. Schematic process of evaluation of signal propagation in an absorbing and refracting medium.

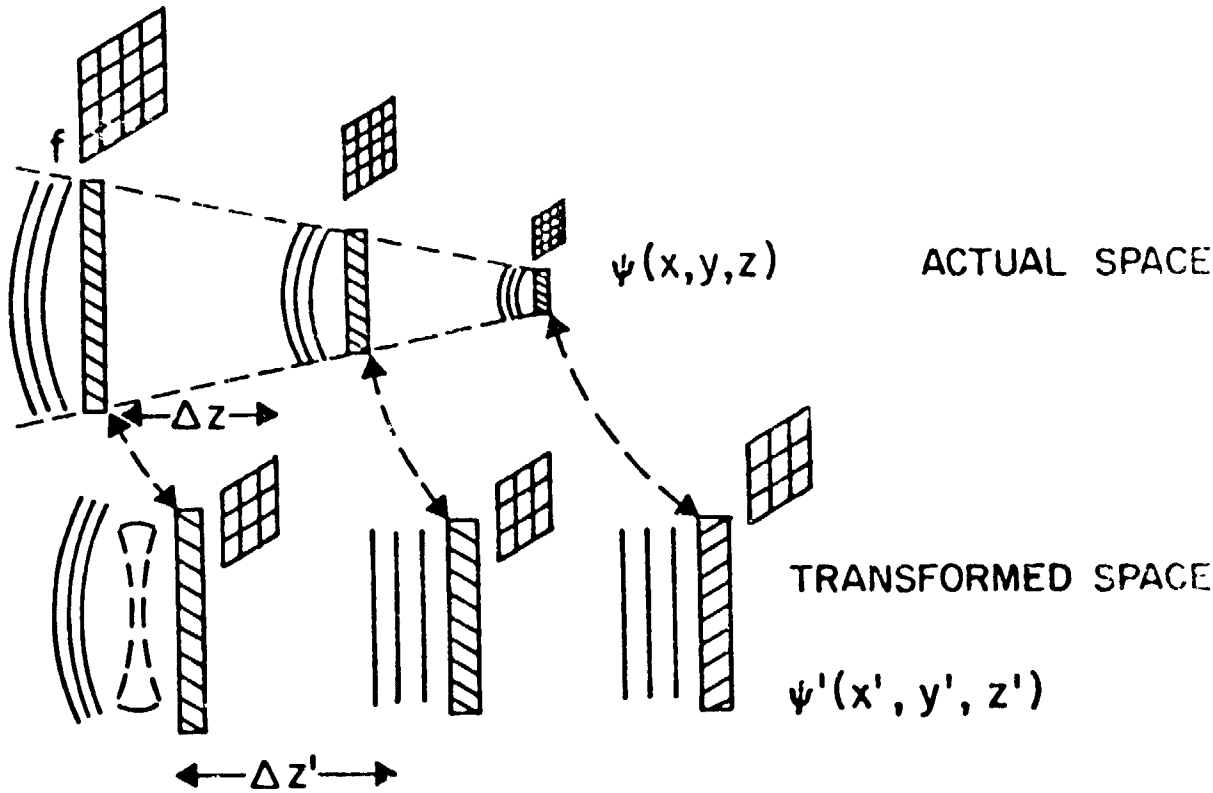

$$\psi(\vec{x}_\perp, z_{n+1}) = \frac{1}{1 - \frac{\Delta z}{z_f}} \psi' \left(\frac{\vec{x}_\perp}{1 - \frac{\Delta z}{z_f}}, z_n + \frac{z_{n+1} - z_n}{1 - \frac{\Delta z}{z_f}} \right)$$

$$\times \exp \left\{ ik \vec{x}_\perp^2 / \left[2 z_f \left(1 - \frac{\Delta z}{z_f} \right) \right] \right\}$$

where

$$\psi'(\vec{x}'_\perp, z_n + \Delta z') = \frac{-i}{\lambda \Delta z'} \iint \psi(\vec{x}''_\perp, z_n) \, e^{-i \frac{k}{2} \frac{(\vec{x}''_\perp - \vec{x}'_\perp)^2}{\Delta z_n}} \, dx'' \, dy''$$

Figure 2. The Talanov Transformation.

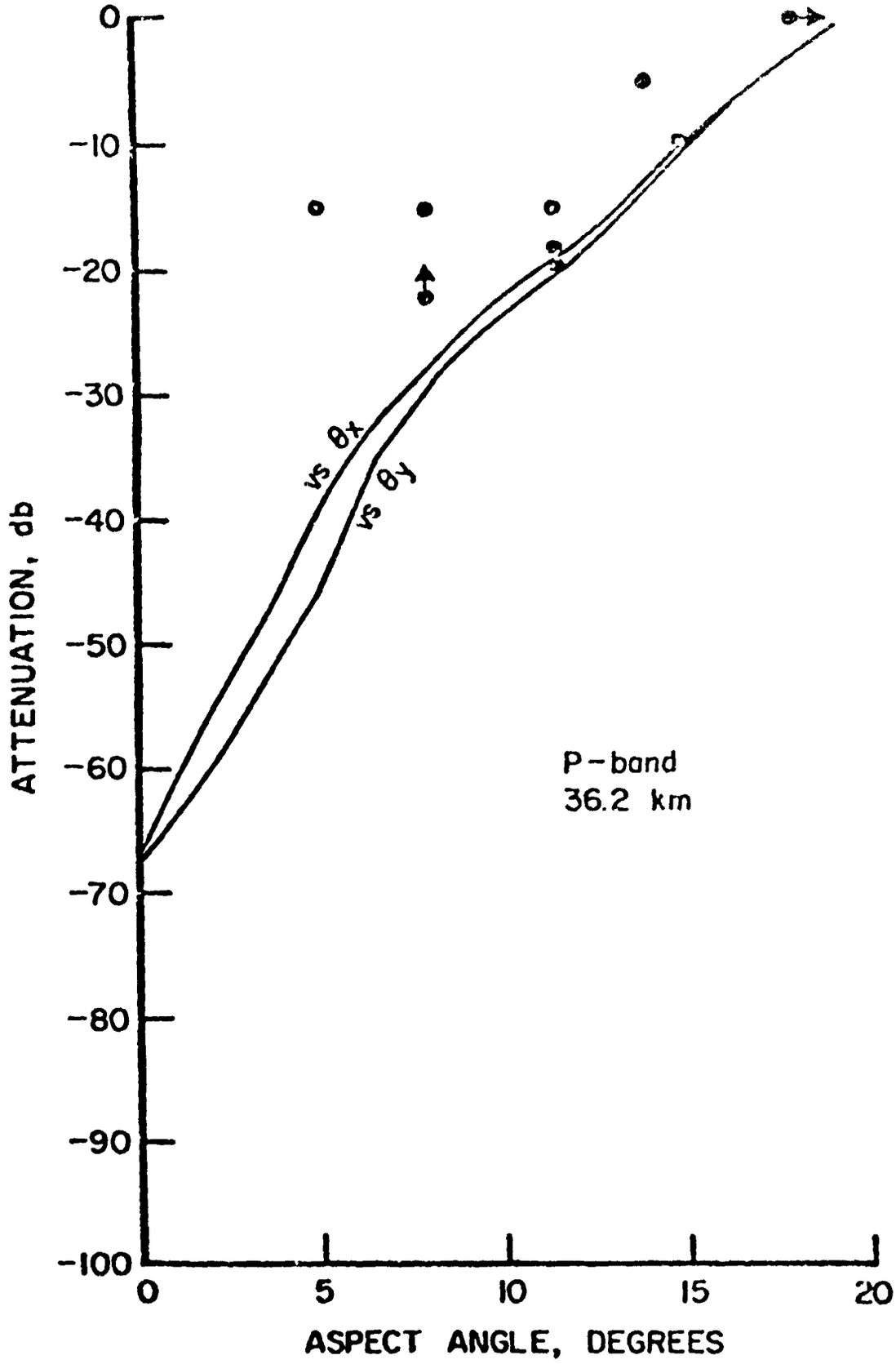

Figure 3. Comparisons between predictions and field measurements: Titan III-C at 36 km, P-band.

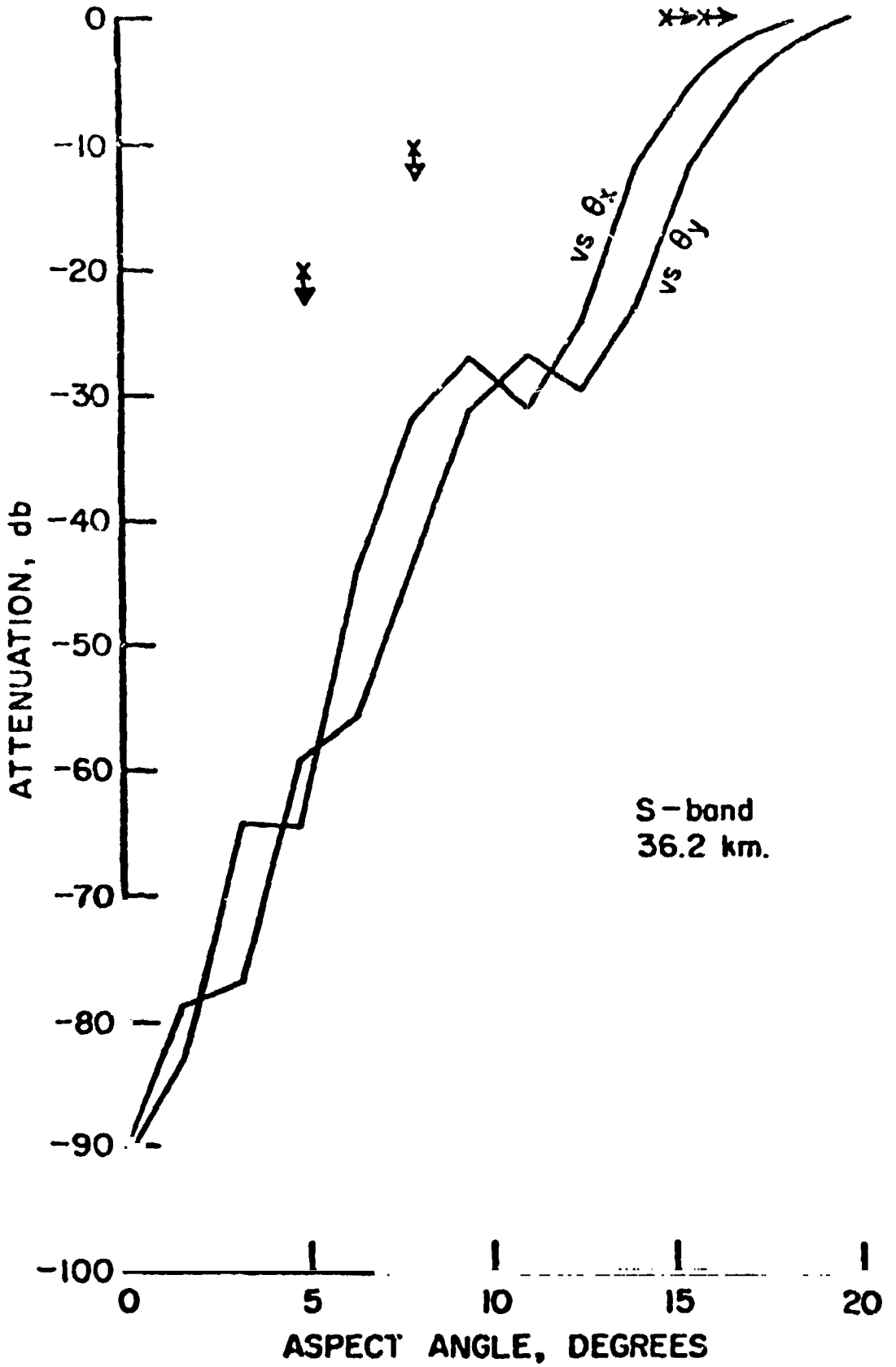

Figure 4. Comparisons between predictions and field data: Titan III-C at 36 km, S-band.

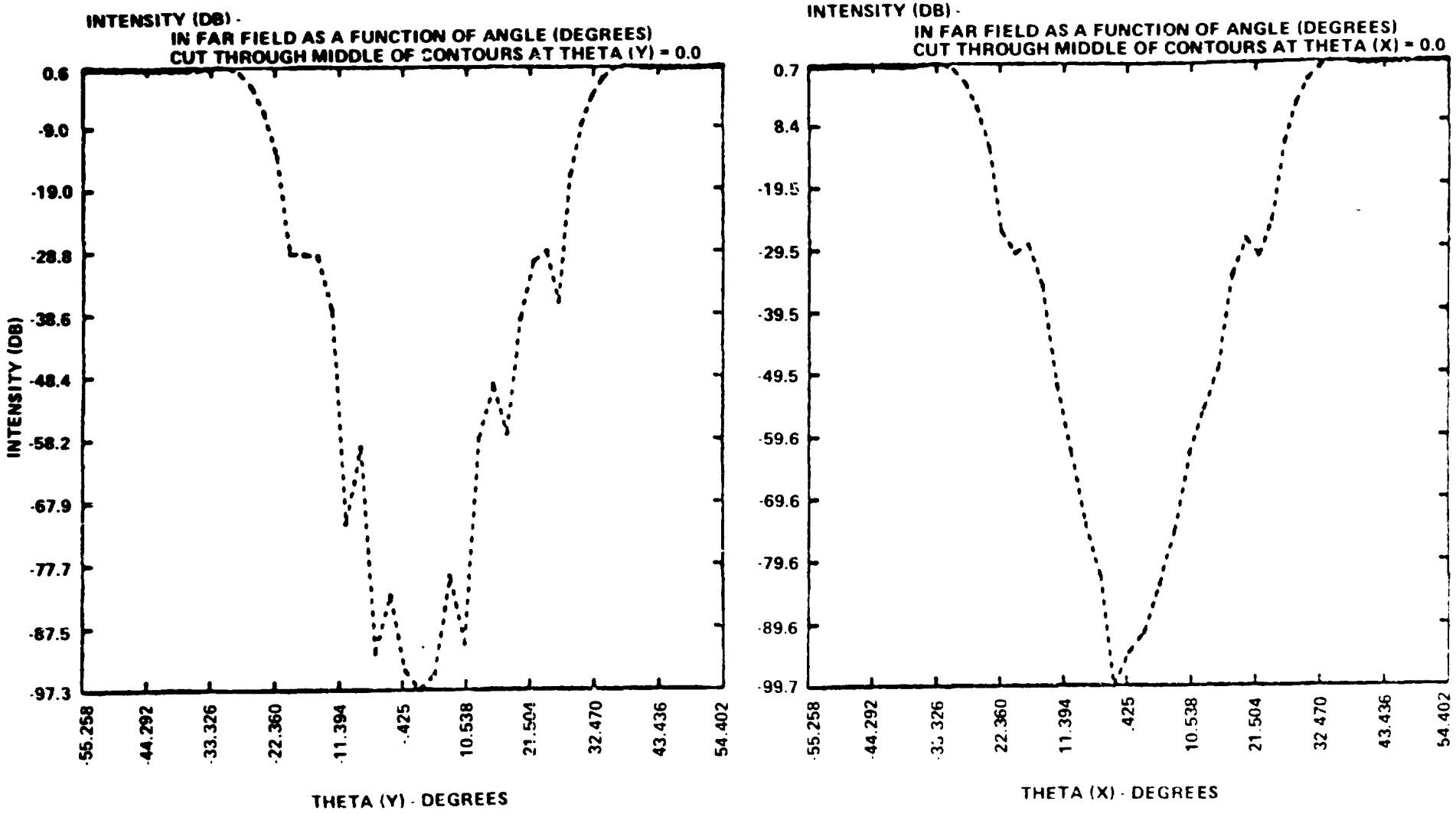

Figure 5. Predicted Space Shuttle range safety signal attenuation as a function of the aspect angles θ_y and θ_x at 37.5 km altitude (SRB antenna).

results imply a marginal condition at the nominal ground site location for northerly launches, but that alternative locations (preferably to the north) provide clear transmission paths to the vehicle (Figure 6).

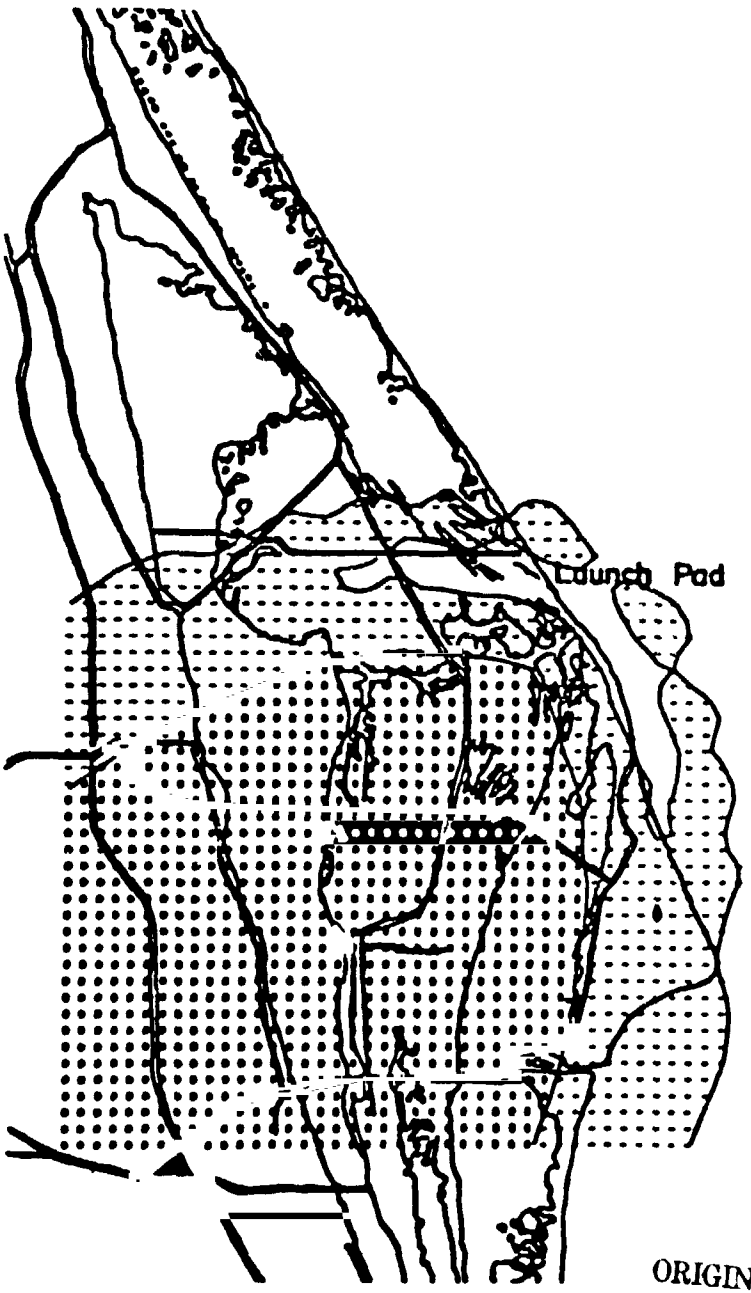

ORIGINAL PAGE IS
OF POOR QUALITY

Figure 6. Received signal strength pattern for various ground stations around Cape Canaveral area for a 37.9° launch azimuth at a vehicle altitude of 37.5 km. Dark shading, $P_s < -94$ db. Light shading, -94 db $< P_s < -84$ db.

3.0 TESTS OF COMPUTATIONAL PROCEDURES AGAINST THEORY

The computer code (FRENL) which performs the calculations outlined in the previous section was furnished to NASA (MSFC) in October 1977 in a form suitable for use on Univac 1108.* In the process of testing this version of the code, we discovered that the computed Range Safety signal level deep in the shadow zone was affected by the mesh spacing of the computation, and that this effect was also present in previous versions of the code. During the initial stages of our previous contract, while coding the original version of FRENL, we had tested the effects of mesh size and found them to be insignificant. Those tests, however, were performed for a much smaller plume than that of the Space Shuttle. It appeared that some aspect of the propagation calculation was being affected by the resolution employed in the calculation, and that this effect was related to plume size, signal wavelength, or some combination of the two.

The effects of resolution on accuracy are most easily tested on a simple problem for which a well-established analytical solution exists. It is also preferable to use a one-dimensional test problem, since ample array sizes can easily be accommodated. Fresnel diffraction by a straightedge (Figure 7) is a suitable test problem. The exact analytical result for the ratio of the intensity I in the presence of a blocking edge to that in the absence of the edge is

$$I/I_o = \frac{1}{2}\left\{\left[C(V) - \frac{1}{2}\right]^2 + \left[S(V) - \frac{1}{2}\right]^2\right\}$$

where C and S are the Fresnel cosine and sine integrals defined as

---

*Previous computations, and the further investigations reported here, were performed on a CDC 7600 at the Lawrence Berkeley Laboratory (Department of Energy).

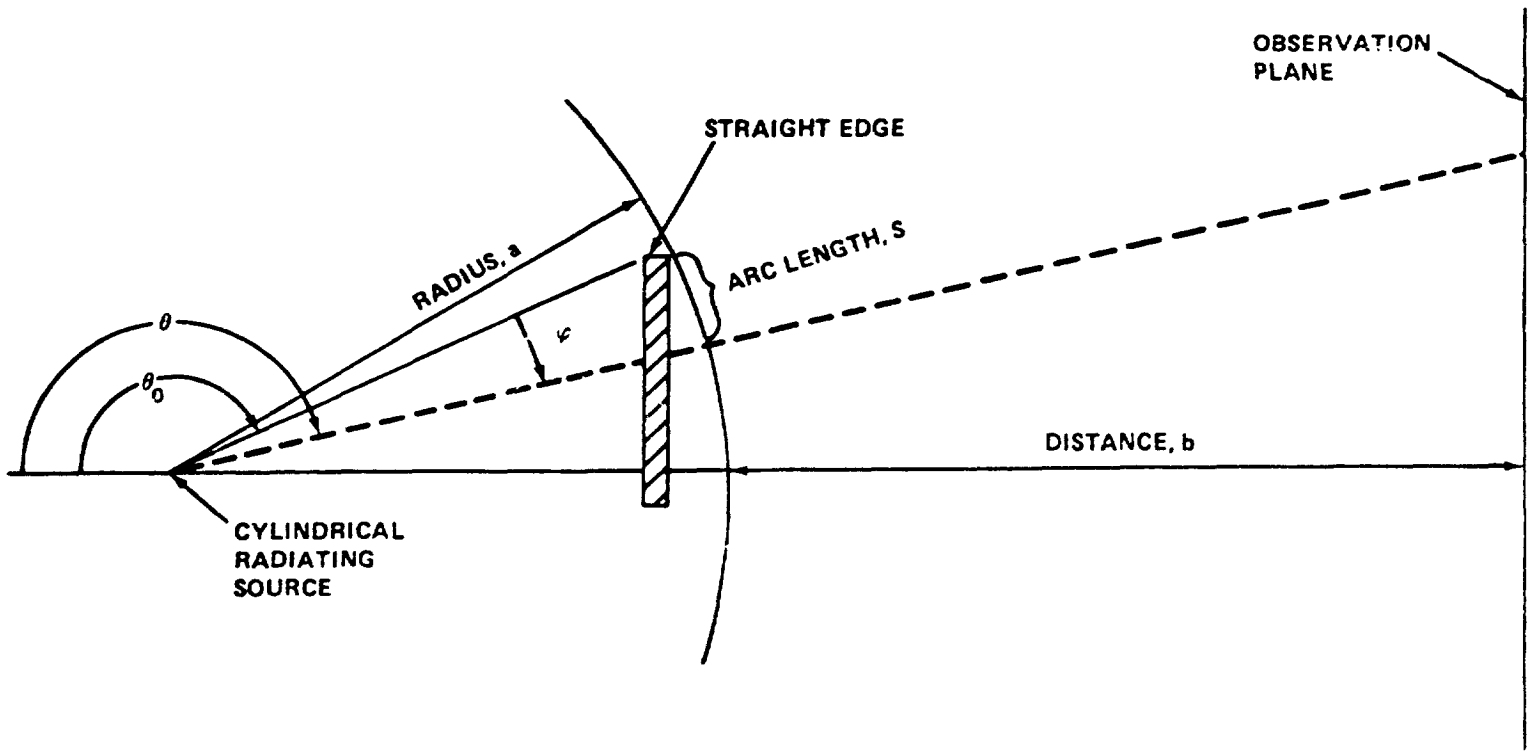

Figure 7. Simplified geometry for straight edge diffraction. From Kalil (1977).

$$C(x) = \int_0^x \cos \frac{1}{2} \pi t^2 \, dt$$

and

$$S(x) = \int_0^x \sin \frac{1}{2} \pi t^2 \, dt$$

with the diffraction parameter V being defined as

$$V = S\sqrt{2(a+b)/ab\lambda} \approx \phi\sqrt{2(a+b)a/b\lambda}$$

The lengths a, b, and S and the angle ϕ are defined in Figure 7. The theoretical intensity pattern is shown in Figure 8; it is the same function used by Vicente (1966) to estimate plume-signal interference. For large V (deep into the shadow zone) the intensity varies as

$$I/I_0 \rightarrow \frac{1}{2} (\pi V)^{-2}$$

To relate this problem to the Space Shuttle interference problem at high altitude, we can estimate the values of V involved there. At tail aspect the angle ϕ is about 1/2 radian, the distance a is of order 75 meters, b is about 50 kilometers, and the UHF wavelength is about 0.75 meters. Thus, at tail aspect

$$V_{max} \approx \frac{1}{2}\sqrt{2x75/0.75} \approx 7$$

Values of V at which we calculated 30-40 db attenuation (which is a significant level in considering transmitter site location) are of the order of 3-5. We must therefore consider the accuracy of our solution for values of V between about 3 and 7.

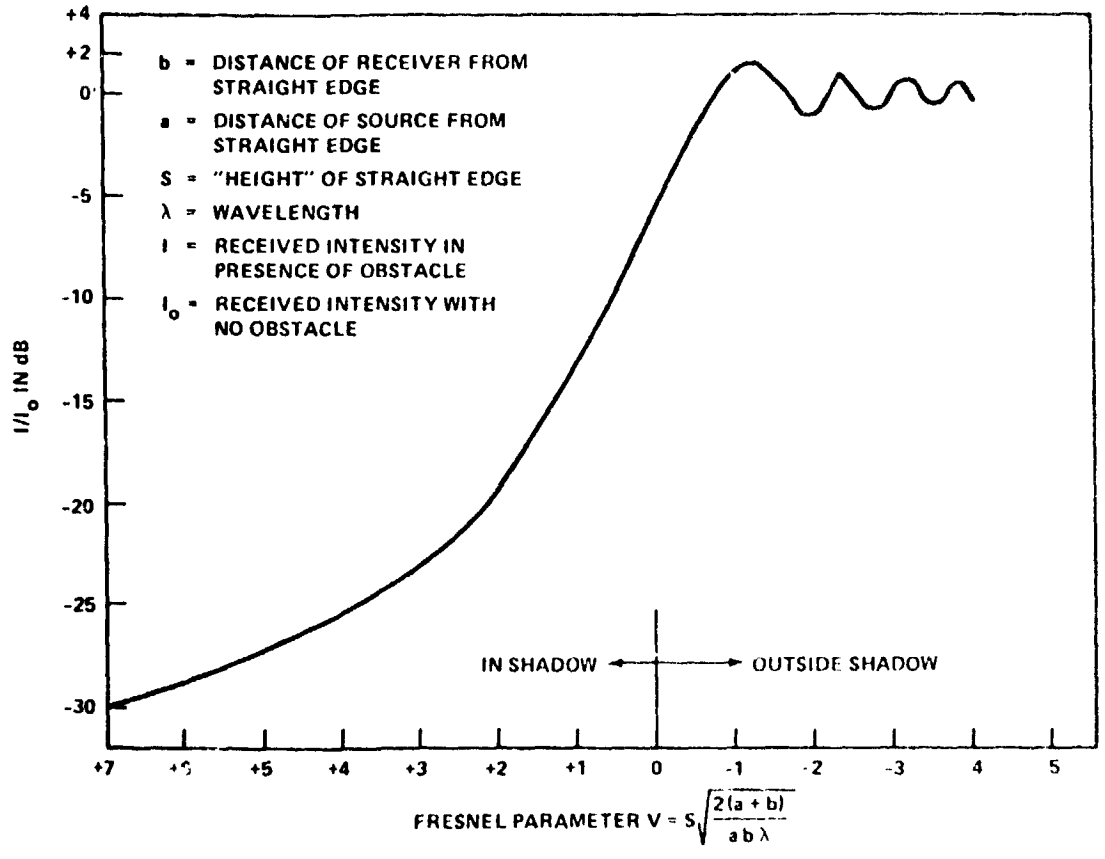

Figure 8. Intensity variations for Fresnel diffraction at straight edge. From Kalil (1977).

Figures 9-11 show the results of applying our computational procedure in one dimension to the straightedge problem for different combinations of signal frequency and mesh spacing. Here $a = 40$ meters, and $b = 260$ meter; these values are roughly appropriate to the ground test conditions, but we extend the calculation to greater angles ϕ than encountered there. In this series of figures the signal frequency is 1/2, 1, and 2 times the nominal Range Safety signal frequency, respectively. The solid line shows the theoretical signal level. The dots, circles, x's, and crosses show the signal level calculated for mesh spacings at the obstacle of 1, 0.5, 0.25, and 0.125 meters, respectively. (The product of mesh spacing and number of points--i.e., the total grid length--is held fixed at 64 meters.) It is evident that problems exist at large mesh spacings, and that a low-resolution calculation can seriously underestimate the intensity in the deeply shadowed region.

This result apparently has to do with the loss of high-wavenumber Fourier components of the signal in the low-resolution calculation. It is these Fourier components which are responsible for the intensity deep in the shadow zone, and their omission appears to result in a less intense signal.

We can systematize these results and develop a criterion for the accuracy of our numerical calculation as follows: In Table I we show the values of the scattering angle ϕ_3, at which the numerical calculation differs from the exact analytical result by 3 db, tabulated against mesh size δx and frequency.

Table I: Scattering Angle ϕ_3

δx	f = 208 MHz	416.5	833
1.0	18°	8.5°	4°
0.5	>30°	16.7°	9.5°
0.25	--	~28°	~18.5°
0.125	--	--	~30

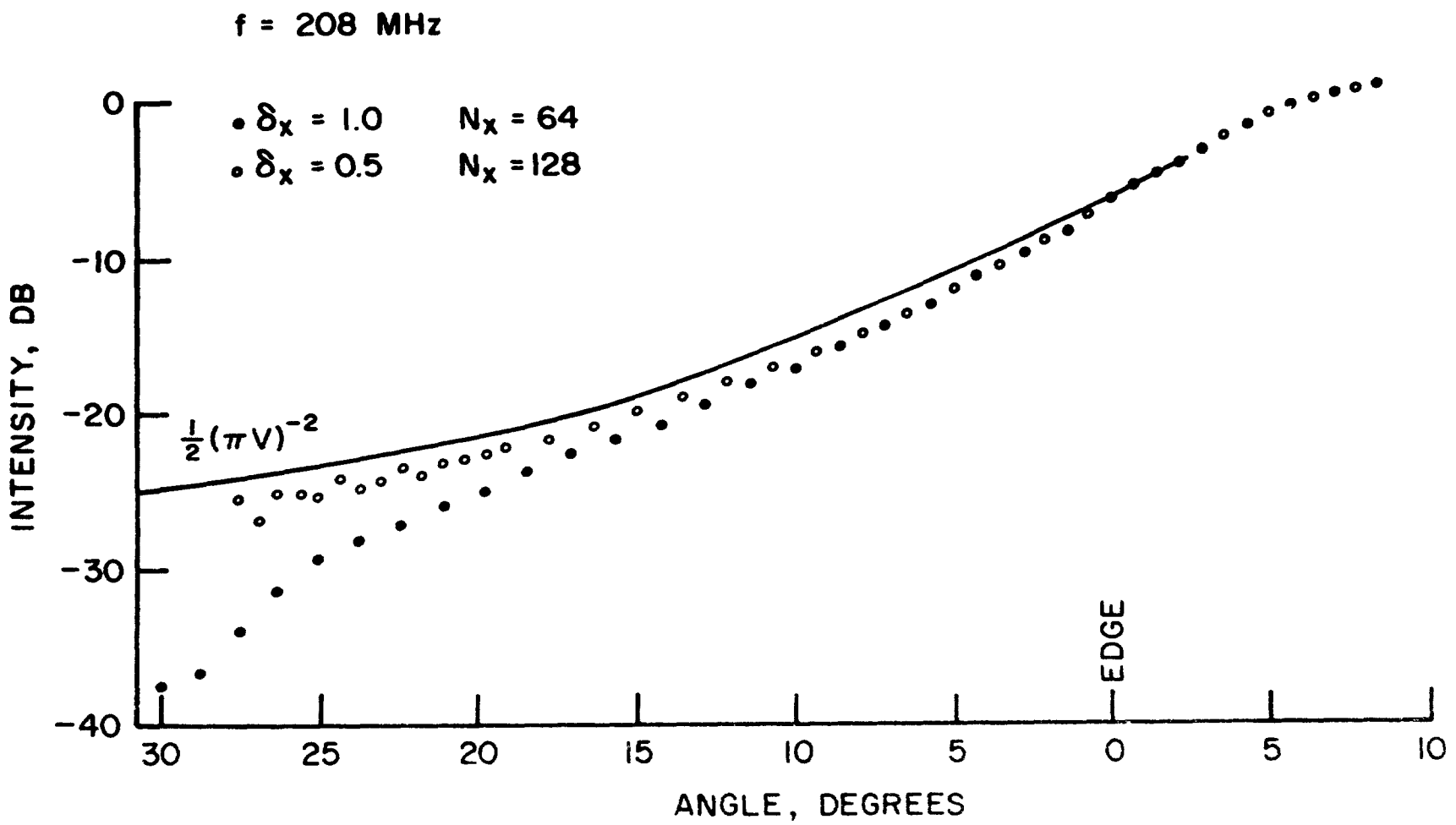

Figure 9. Computed diffraction by a straightedge (a = 40 m, b = 260 m) for f = 208 MHz. Solid line shows theoretical value, points show numerical results for indicated mesh spacings.

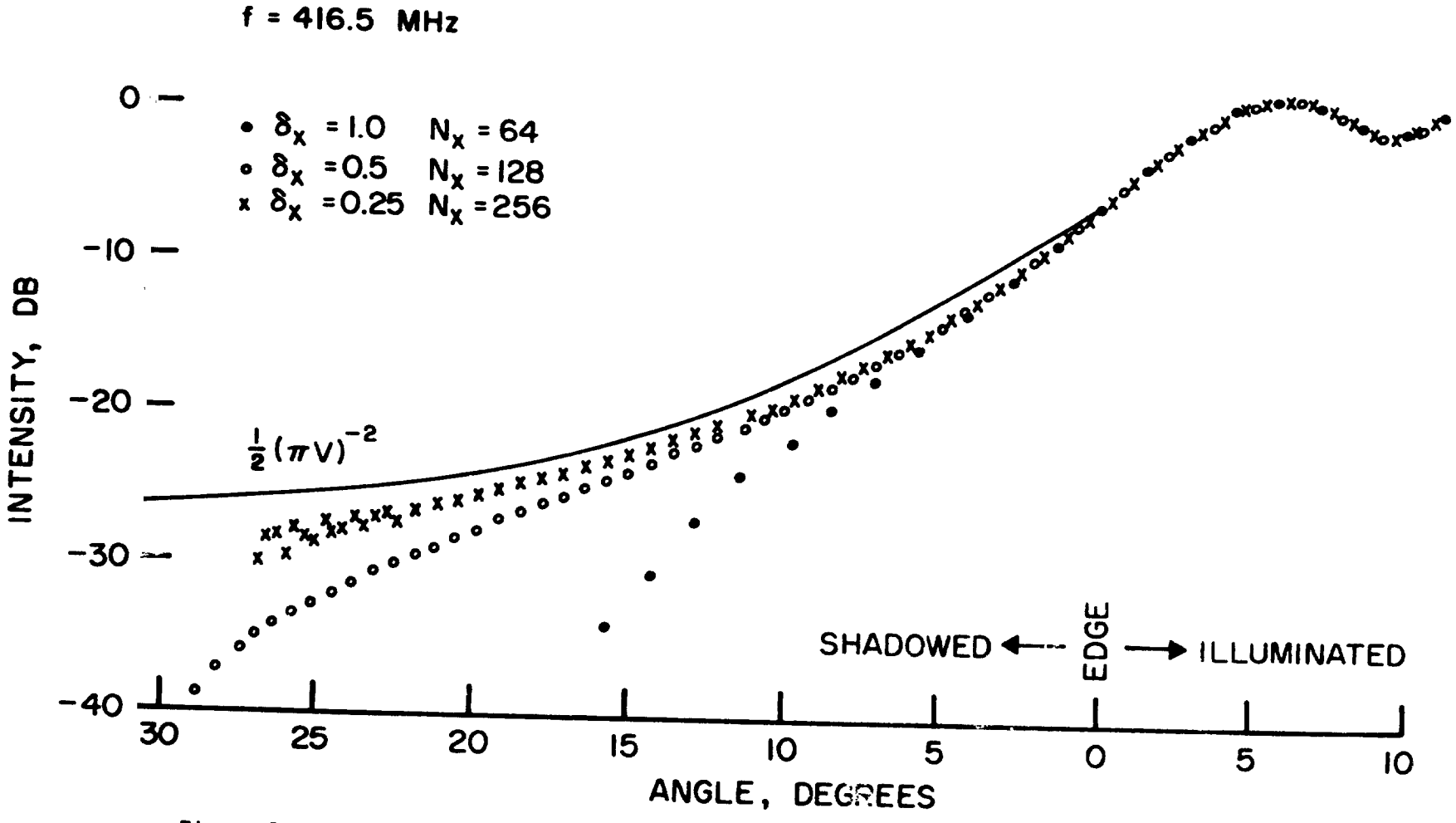

Figure 10. Computed diffraction by a straightedge (a = 40 m, b = 260 m) for f = 416.5 MHz. Solid line shows theoretical value, points show numerical results for indicated mesh spacings.

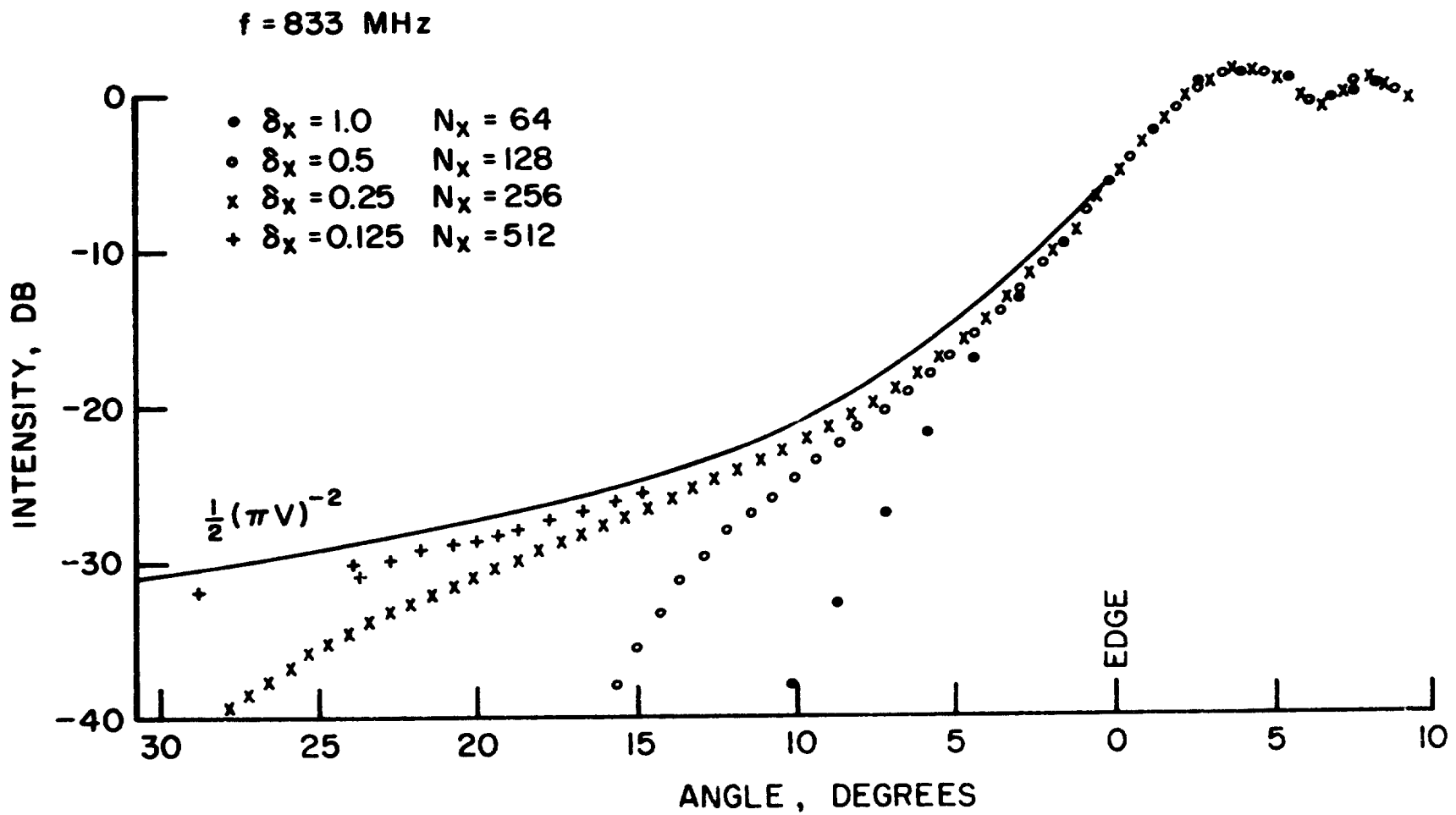

Figure 11. Computed diffraction by a straightedge (a = 40 m, b = 260 m) for f = 833 MHz. Solid line shows theoretical value, points show numeerical results for indicated mesh spacings.

Within the scatter of this limited amount of data we find that

$$\phi_3 \sim \lambda/\delta x$$

and a proportionality constant of about 0.2. This is consistent with an accuracy criterion based on resolving the first unobserved Fresnel zone in the vicinity of the edge. The radius of the n^{th} zone is

$$r_n = \left(\frac{\lambda abn}{a+b}\right)^{1/2} \approx S$$

and its width is approximately (since $\Delta n = 1$)

$$\Delta r_n = \left(\lambda \frac{ab}{a+b}\right)/(2S) = (\lambda Z'/2S)$$

Thus, at the edge

$$\Delta r_n = \lambda/2\phi$$

A reasonable criterion for accuracy in this numerical calculation is that the first Fresnel zone at the edge of the blocking surface be resolved in the Nyquist sense of being able to fit one complete Fourier mode with $\lambda_{mode} = 2\delta x$ within this zone, or

$$\delta x \approx \frac{1}{2} \Delta r_n \approx \frac{1}{4} \frac{\lambda}{\phi}$$

Satisfying this criterion leads to 3 db accuracy in the deeply shadowed zone.

In the case of the Space Shuttle Range Safety signal, the wavelength is 0.72 meters and the tail-aspect scattering angle is of the order of 0.5 radians, so that an accurate calculation requires a mesh spacing

$$\delta x \approx 0.72/(4 \times 0.5) = 0.36 \text{ meters}$$

The actual mesh spacing of our previous calculations was about 3 meters at the point where the tangent ray from the antenna skims the plume. We conclude that our Shuttle calculations are overly conservative at scattering angles greater than 0.06 radians, or at tail aspect angles less than about 22°. Table II gives an estimate of the mesh size and number of grid points necessary for an accurate calculation as a function of scattering angle:

Table II: Mesh width and grid size requirements versus scattering angle

Scattering angle ϕ	Mesh width, δx	Grid size
0.06	3	64x64
0.2	0.9	256x256
0.5	0.36	1024x1024 (512x512?)

Since the computation time is approximately proportional to the number of mesh points N (N $\log_2$N for the FFT operations, N for the phase change calculations), an accurate calculation at tail aspect would require of the order of at least 100 times the cost of our previous calculations. The figure is probably somewhat greater if one accounts for the increased overhead associated with storage and transposition of large (1 to 4 million words) arrays on disc.

In the case of the ground tests, our accuracy criterion can be satisfied at all tested frequencies. In the next section we compare our computation using the FFT procedure with the test results.

4.0 GROUND TEST CALCULATIONS

For the ground-based SRM firings at Thiokol, the receiving and transmitting antennas were located so that the line-of-sight lies at an angle to the plume centerline. An aerial view of the test setup is shown in Figure 12; the positions of the SRM test stand, plume centerline, and transmitting and receiving antennas are indicated. The interval between ground contour elevations is 25 ft., and the motor fires toward a hill.

Kalil has summarized the conditions encountered during the motor firing. The motor plume scours out a cavity in the ground, and appears to require about 30-40 seconds to assume a steady state. A large dust cloud is formed where the plume impinges upon the hill. The dust cloud appears from the photographs in Kalil's report to be clear of the nominal transmission path, and is not included in our calculation.

We have employed plume properties calculated by the Lockheed Missiles and Space Company, Huntsville Research and Engineering Center. The computer program used to generate these results is one which was also employed in calculating the plume properties used in our previous calculations for in-flight attenuation. It provides values of collision frequency and electron density as a function of radial distance from the plume axis on a series of planes normal to the axis. The 10^9 cm^{-3} electron density contour (at which $n_i \approx 0.003$ at 416.5 MHz, leading to an attenuation of 0.11 db between successive phase screens) is shown as a function of axial distance in Figure 13; the plume shape deduced by Kalil from photographs taken during the test is also shown for comparison.

There is a notable difference in shape between the electrical plume and the visible plume. The latter is due to aluminum oxide particles formed in the combustion process inside the motor. Upon leaving the motor the particle-laden exhaust gases mix with ambient air. Because the oxide particles do not react, the edge of the opaque

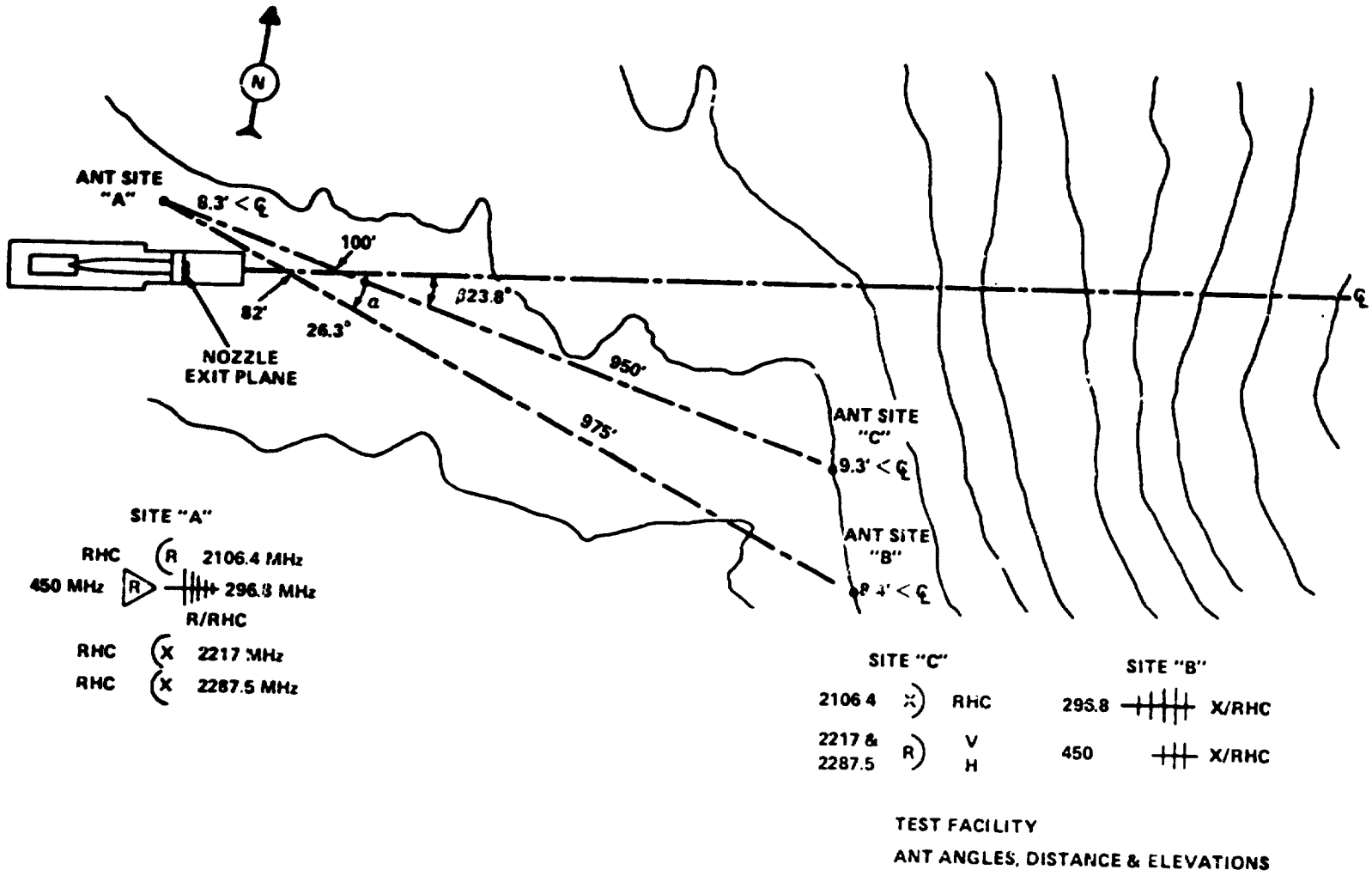

Figure 12. Plume test set-up. From Kalil (1977).

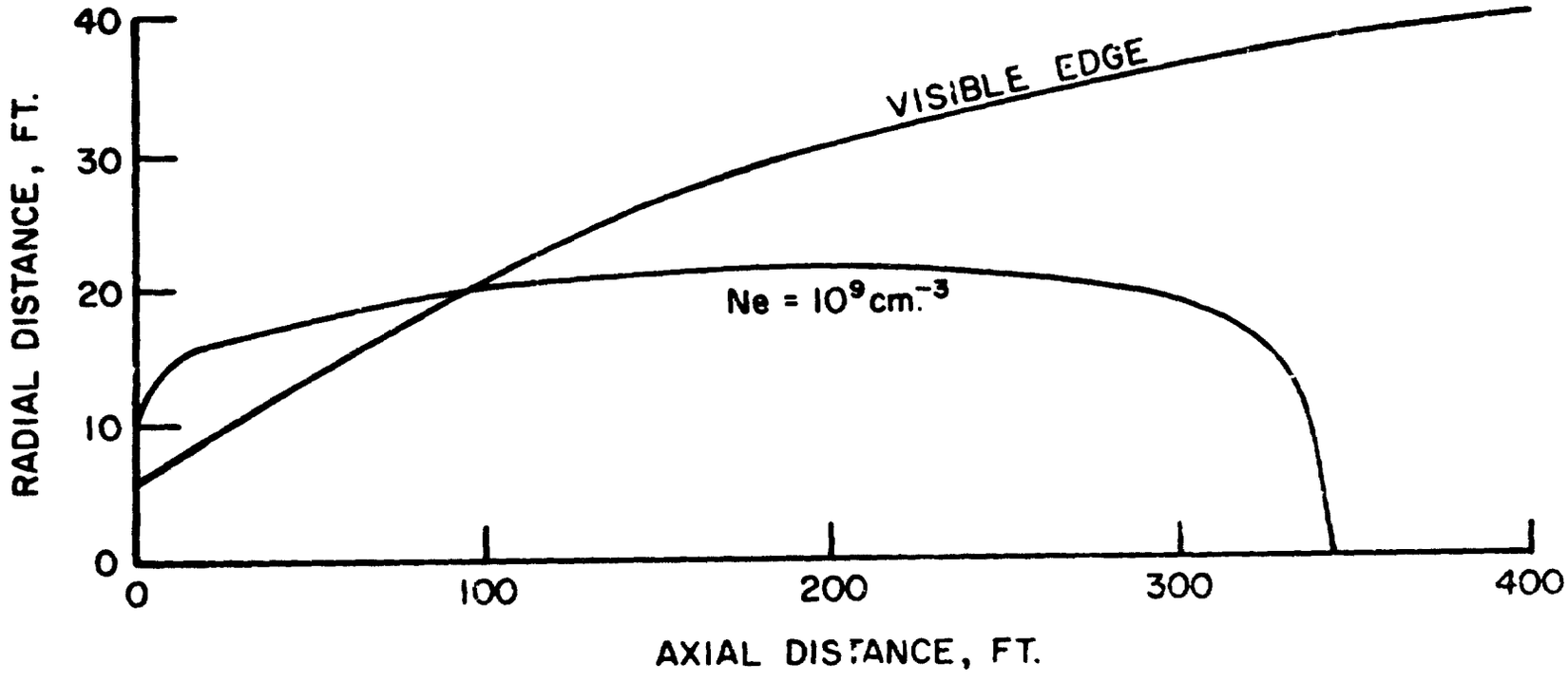

Figure 13. Comparison of computed electrical plume (contour of electron density $N_e = 10^9$ cm^{-3}) with visible plume shape deduced from photographs.

region gets further away from the plume centerline until the cloud as a whole begins to become transparent. Dilution of the particle cloud in the first several hundred feet is apparently insufficient to allow the apparent visible edge to bend over toward the axis. The electrons, on the other hand, react in the outer regions of the plume. Electron production by afterburning appears to peak in the first 200 ft. or so and from then on electron concentrations decrease as the result of both mixing and recombination and attachment processes. This difference in physical processes defining the electrical and visible plumes probably has much to do with shape differences in the downstream regions. Interactions with the ground may also be significant. The reasons for the discrepancies in the first 80 ft. are less physically obvious, and may be the result of excess diffusion in the Lockheed calculation* or of problems in interpreting the plume photographs. The "edge" locations are comparable in the region (80-100 ft.) where the line of sight intercepts the plume.

The major adaptation of the FRENL code to allow calculation of signal levels for the test conditions was removing the assumption that the nominal propagation path parallels the plume axis. It was necessary to interpolate between the planes on which the plume data were provided in order to evaluate the plume's refractive index on planes normal to the nominal (angled) propagation path. As one proceeds from one phase screen to the next along this path, one encounters the plume at different locations; looking toward the receiver along the path, the intercepted portion of the plume moves from right to left as one views phase screens successively further from the transmitter. Examples of the development of the propagation calculation will be shown subsequently.

If one treats the plume edge as an effective straightedge in the region near where the transmission path crosses the plume axis, one can evaluate an effective value of the scattering angle for the

*The LAPP code on which the LMSC calculation is based has been shown (Dash and Pergmanent, 1977) to calculate anomalously high diffusion rates near the initial plane.

test conditions and estimate the mesh size required for computational accuracy in the FFT mode. These parameters are summarized in Table 3-7 of Kalil's report; the effective scattering angle is about 0.1 radian. The corresponding required mesh sizes at UHF (λ = 0.72 m) and S-band (λ = 0.14 m) are 1.8 m and 0.35 m, respectively. It is relatively easy to fulfill this requirement at UHF with the nominal 64x64 grid used in FRENL. The range safety signal experiment does not provide a critical test of our computational procedure as such. The S-band experiment is at best marginal for this purpose, and it will be difficult to distinguish errors arising from our computational technique from those associated with inaccurate descriptions of the plume and the environment.

The development of the calculation at 416.5 MHz in the absence of ground effects is shown in Figures 14 and 16. (This calculation is equivalent to placing a perfectly reflecting ground plane along the line of sight between transmitter and receiver.) The coordinate system is chosen as follows: the z axis points from the "transmitter" (Kalil's site A) toward the receiver (Kalil's site B or C), and the y axis points upward. The x axis completes a left-hand coordinate system; it points toward the plume. The mesh spacing in the x (horizontal) direction is generally 3 to 5 times the spacing in the y (vertical) direction in order to take in more of the long axis of the plume. According to the data given by Kalil, the line of sight is a short distance (0.5 m) above the plume axis, so that the calculation is not quite symmetric about the x axis.

Figure 14 shows contours of imaginary parts of the refractive index on the second, fifth, and thirteenth phase screens, representing angled cuts through the plume at stations progressively further downstream. Because of the difference in mesh spacings in the x and y directions, these contours appear compressed in the x direction. They are actually ellipses with the major axis parallel to the x axis. The apparent shrinkage of the plume as one progresses downstream is a consequence of the growth of the computational mesh in accordance with

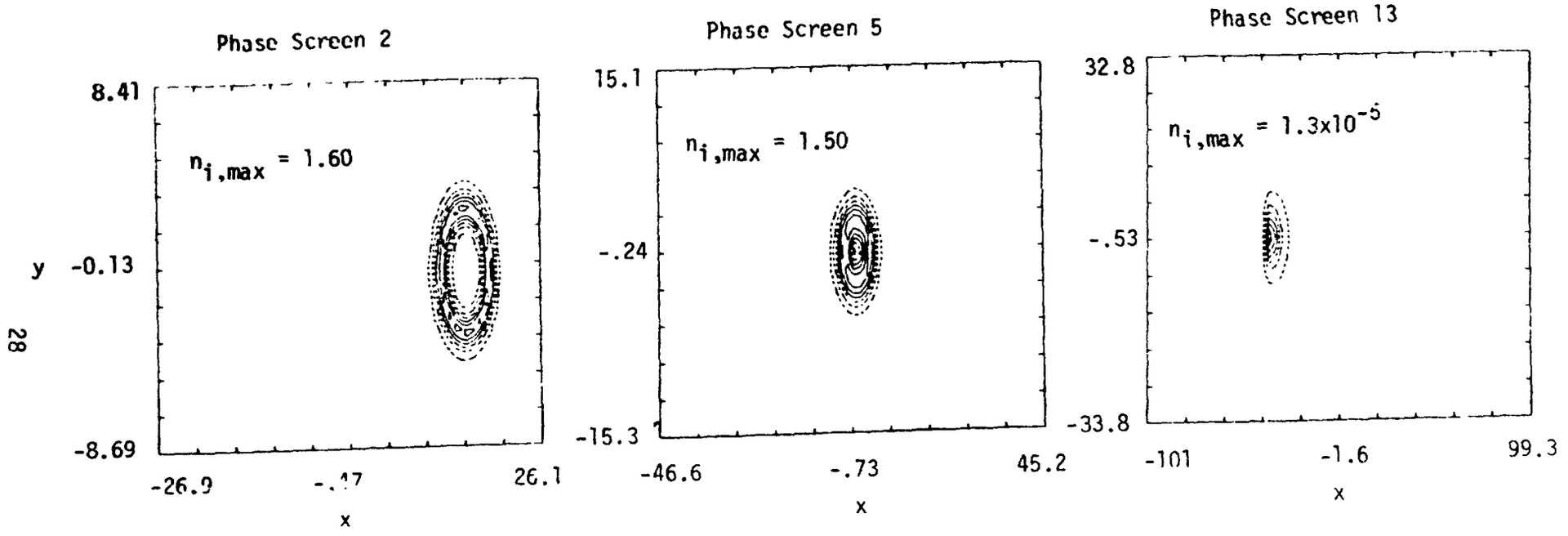

Figure 14. Contours of imaginary refractive index for f = 416.5 MHz on cuts through SRM plume on indicated phase screens. Grid dimensions in meters. Note different x and y scales. Ground interference neglected.

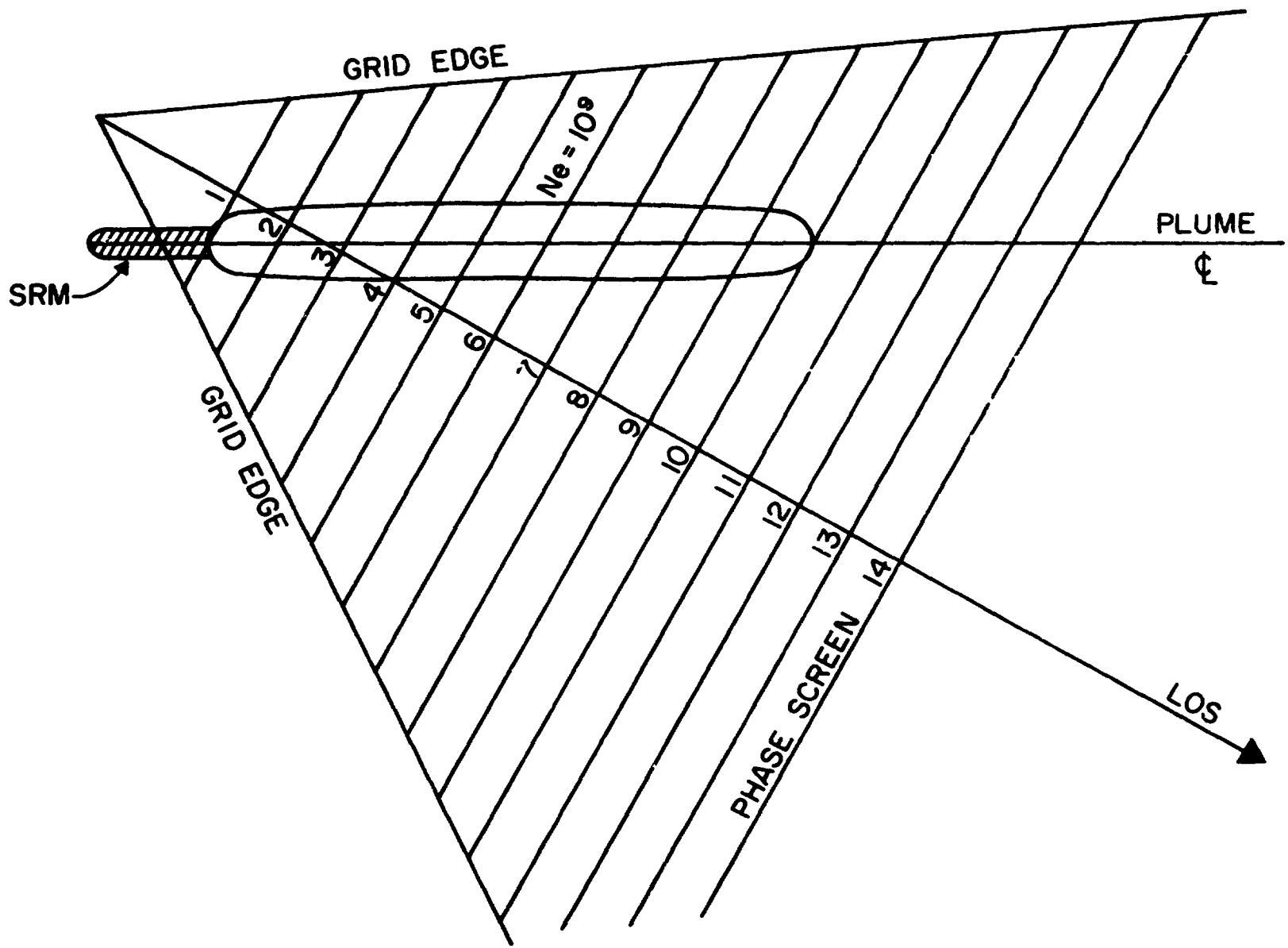

Figure 15. Sketch of geometry of propagation calculation viewed from above showing SRM, plume (defined by contour of selection density = 10^9 cm^{-3}), edges of computational grid in x direction, and successive phase screens at which plume attenuation is evaluated.

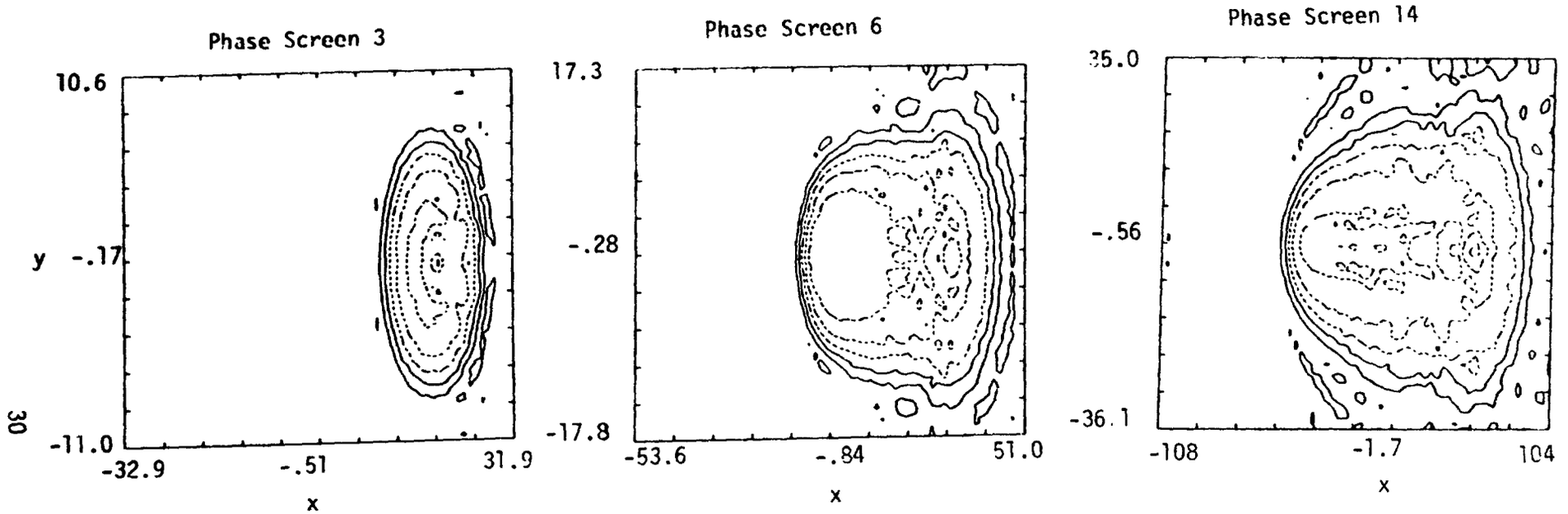

Figure 16. Contours of magnitude of field amplitude $|\psi|$ for f = 416.5 MHz incident upon the indicated phase screens. Grid dimensions in meters. Note different x and y scales. Ground interference neglected.

the Talanov transformation. The propagation geometry (viewed from above) is sketched in Figure 15. We have used the 10^9 cm^{-3} electron density contour to indicate the strongly absorbing part of the plume. Contours of constant field amplitude ψ are shown in Figure 16. At the right of the figures, the wave has passed upstream of the nozzle exit plane; since we have not accounted for interferring structures, the wave is unattenuated. At the left of the figures, the wave has either not yet reached the plume or has passed downstream of the region of large electron density. These regions are far enough from the line of sight so that their contribution to the transmitted signal is small with respect to the signal diffracted around the edges of the plume (in the y direction).

We have accounted for the effects of the ground by placing a perfectly absorbing medium 3 meters below the line of sight. In actuality the ground will be somewhat reflective, and scattering rom irregularities at the surface will be significant. Different reflectivities and scattering coefficients should be expected for the horizontal and vertical polarization components; these polarization effects cannot be included in a scalar wave treatment. A more sophisticated treatment of ground effects is possible but would require a great deal of effort to implement. Imposition of an absorbing ground plane produces some attenuation of the signal in the absence of the plume due to diffraction effects near the ground. We calculate the plume-induced attenuation as the difference between signal levels in db with and without the plume.

Figure 17 shows the Range Safety signal intensity as a function of angle in a plane normal to the ground at the location of the receiver with (bottom) and without (top) the SRM plume. Effects at the edges (angles greater than ±8 to 9 degrees) are the result of aliasing and should be discounted. Values at angles less than -0.55 degrees are actually below ground level and should be discounted. The signal level relative to free-space propagation without the plume at the receiver location ($\theta_y = 0$) is -2.2 db. The signal level with the

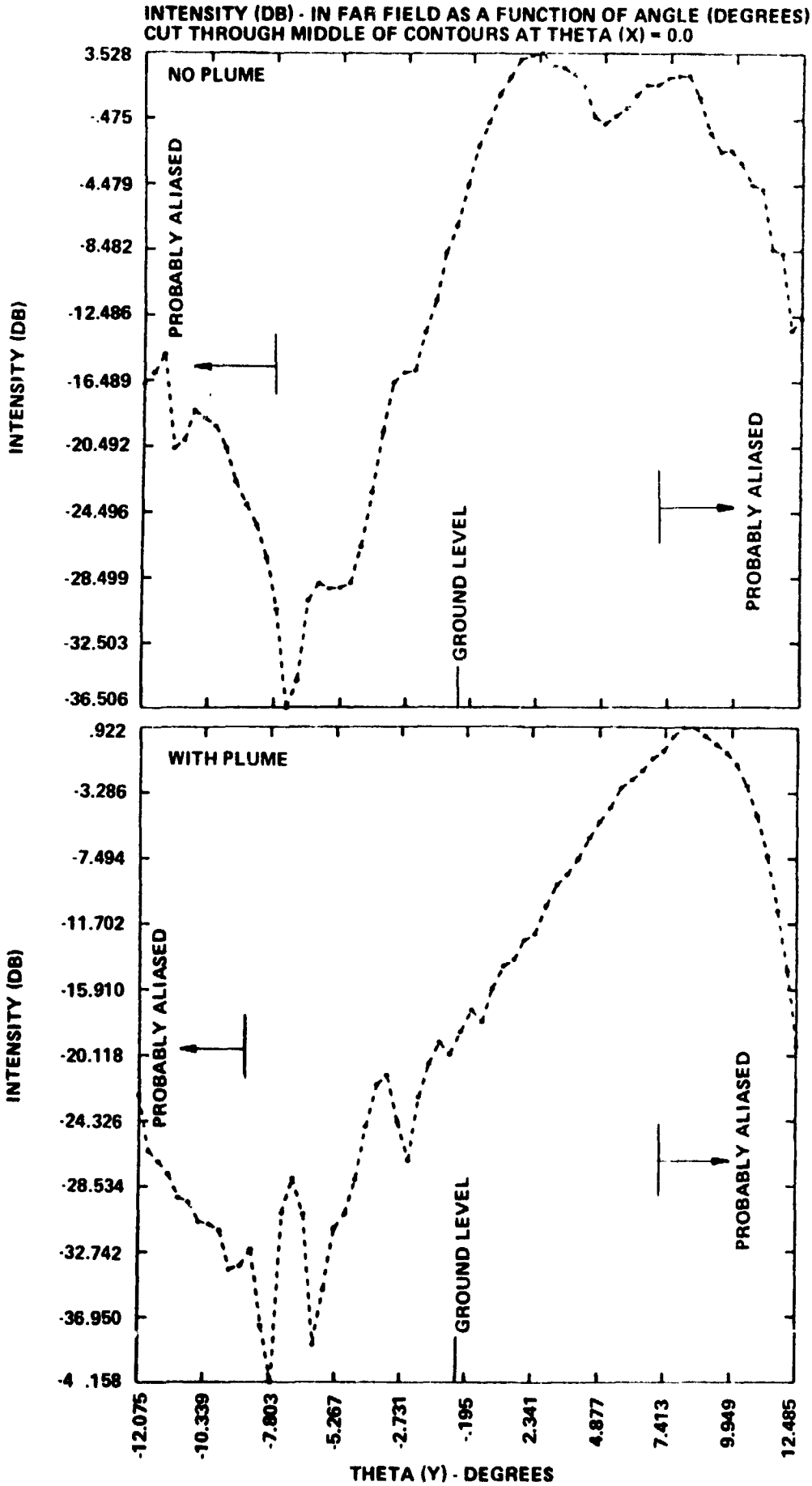

Figure 17. Intensity as a function of vertical angle in receiver plane at 416.5 MHz. Ton, no plume; bottom, with plume. Angle scale is same for each graph. (I vs. θ_y)

plume is -17.2 db. The plume-induced attenuation is 15 db, a figure in excellent agreement with the measured values reported by Kalil.

The mesh spacing δy near the place where the plane $x = 0$ cuts through the plume axis is about 0.5 meters. We calculated previously that our Fresnel zone criterion of accuracy would be satisfied for a mesh size of 1.8 meters. We are therefore operating in a regime where we expect good results from the numerical calculation.

We have also calculated the plume-induced signal attenuation at S-band. Our calculations are for the 2106 MHz circularly polarized signal, to which one scalar wave treatment should be applicable. Even at this higher frequency there is no great difficulty in satisfying the accuracy criterion for the mesh spacing δy in the region where the line of sight crosses the plume; larger meshes occur at subsequent phase screens because of beam divergence, but they are less directly relevant to the more one-dimensional behavior near $x = 0$. We therefore expect that the propagation calculation should be accurate.

Because the S-band antennas produce a narrow beam (in contrast to the nearly isotropic Range Safety antenna), it is necessary to include the antenna pattern in the calculation. The antenna pattern used is based on Kalil's Figure 3-5; the low-power sidebands (required only in the x direction because of the narrower grid in the y direction) were neglected. The antenna pattern was extrapolated using a Gaussian falloff with angle. The antenna pattern (amplitude $|\psi|$) is shown in Figure 18. Free-space propagation of this pattern from the first phase screen to the receiver produces only small changes at angles less than 6-8°, so that we can consider the pattern to be fully developed in the main lobe at the initiation of our calculations.

The intensities in the plane $x = 0$ (vertical along the line of sight) at the receiver location are shown as functions of angle θ_y with and without the plume in Figure 19. In this case the difference between signal levels in db with and without the plume is 49 db. This

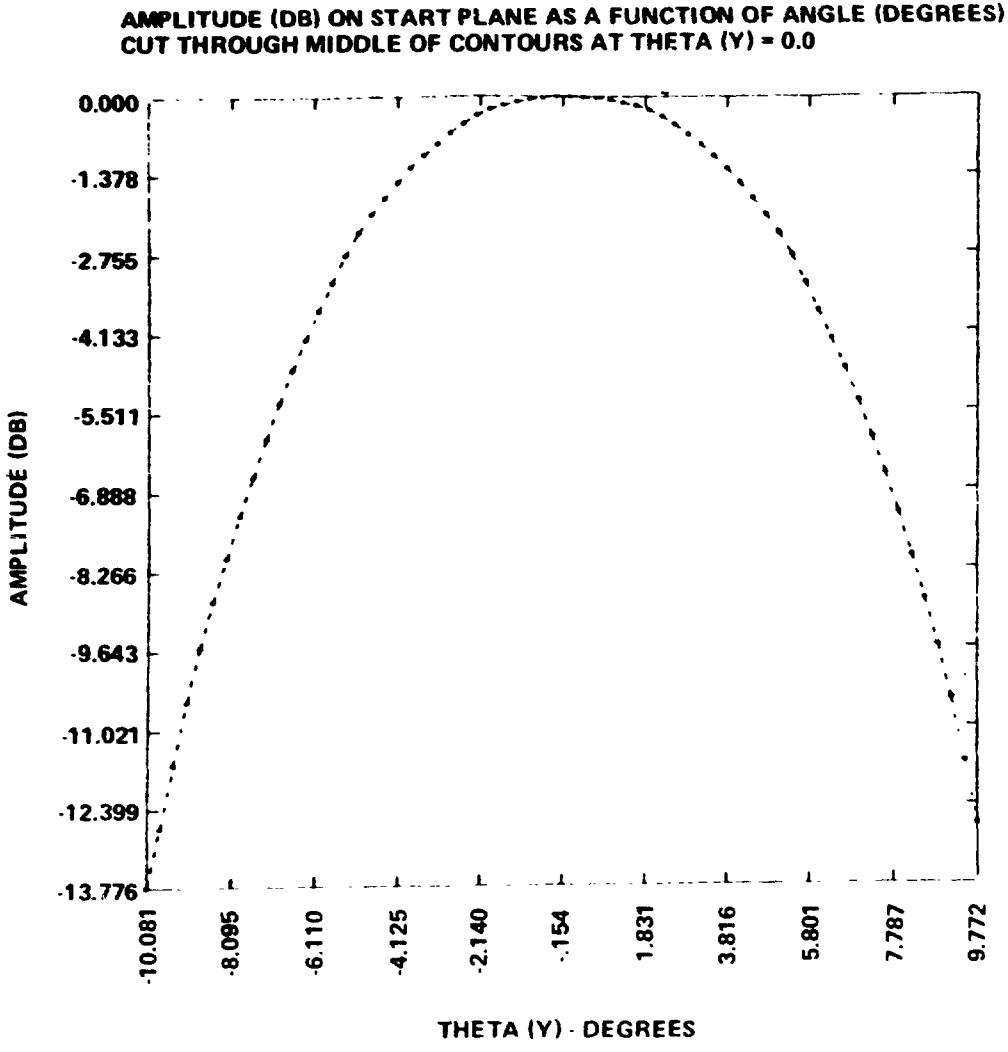

Figure 18. S-band antenna pattern (field amplitude $|\psi|$) used in calculations.

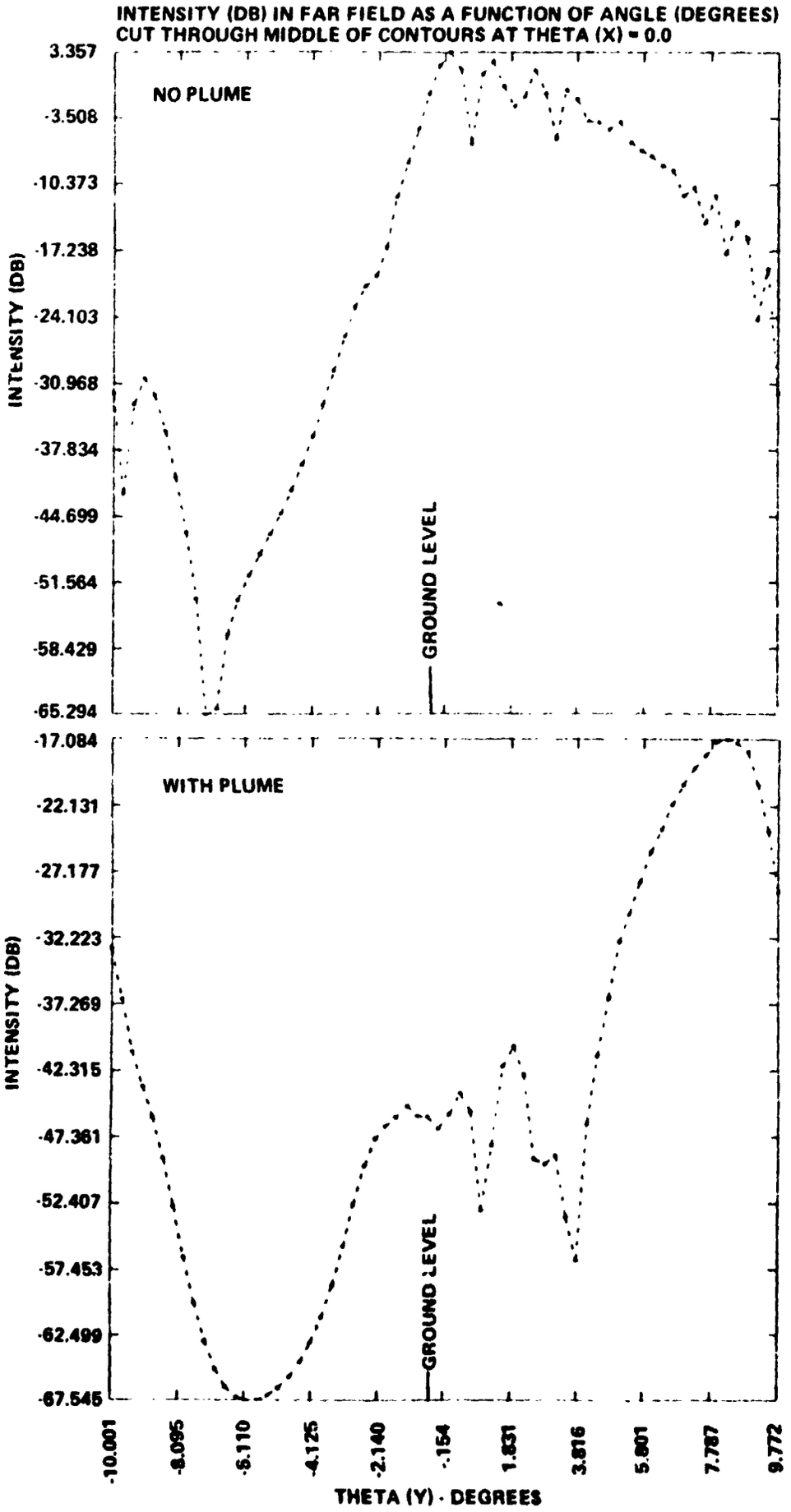

Figure 19. Received S-band (2106 MHz) signal intensity as a function of angle in vertical plane. Top, no plume; bottom, with plume. (I vs. θ_y)

attenuation is considerably higher than the measured attenuation of 36 to 20 db. (The S-band signal attenuation decreases somewhat during the motor burn.)

We have not been able to explain the discrepancy between the observed and predicted S-band attenuation levels. Reasonable changes in transmitter location or ground plane location change the predicted attenuation by a few db, but not enough to reconcile the calculation with the measurements. Changes in plume properties (e.g., centerline elevation) great enough to bring observation and measurement into agreement would destroy the good agreement found for the Range Safety signal. On the basis of results reported in the previous section, it is difficult to ascribe the entire discrepancy to errors in the propagation calculation.

A possible explanation may lie in differences between the electrical properties of the actual fluctuating turbulent plume and those of the mean flow field. It is often observed that turbulent media affect electromagnetic waves as if the instantaneous gradients in electron density were much sharper than those of a time-averaged medium. Such local sharpening can be observed in the realizations of the turbulent electron density fields of high-altitude plumes presented in our previous report (Boynton, et al., 1977a). In Figure 20 we plot the field amplitude $|\psi|$ at $x = 0$ emergent from the fifth phase screen. (Further attenuation or refraction beyond this point is negligible along this plane.) The quantity plotted is the ratio of the magnitude of ψ to its magnitude at the center $(x = y = 0)$ of the first phase screen 18 meters from the transmitter. The region at angles below 7.4°, where plume attenuation is significant, is seen to have a tail extending into the nominally shadowed region. The mean plume has a "fuzzy" edge; the emergent wave lacks the high spatial wavenumber Fourier components which produce the signal deep in the shadowed region in the case of a sharp edge. If the plume were actually a series of sharper-edged structures, with the edge position fluctuating

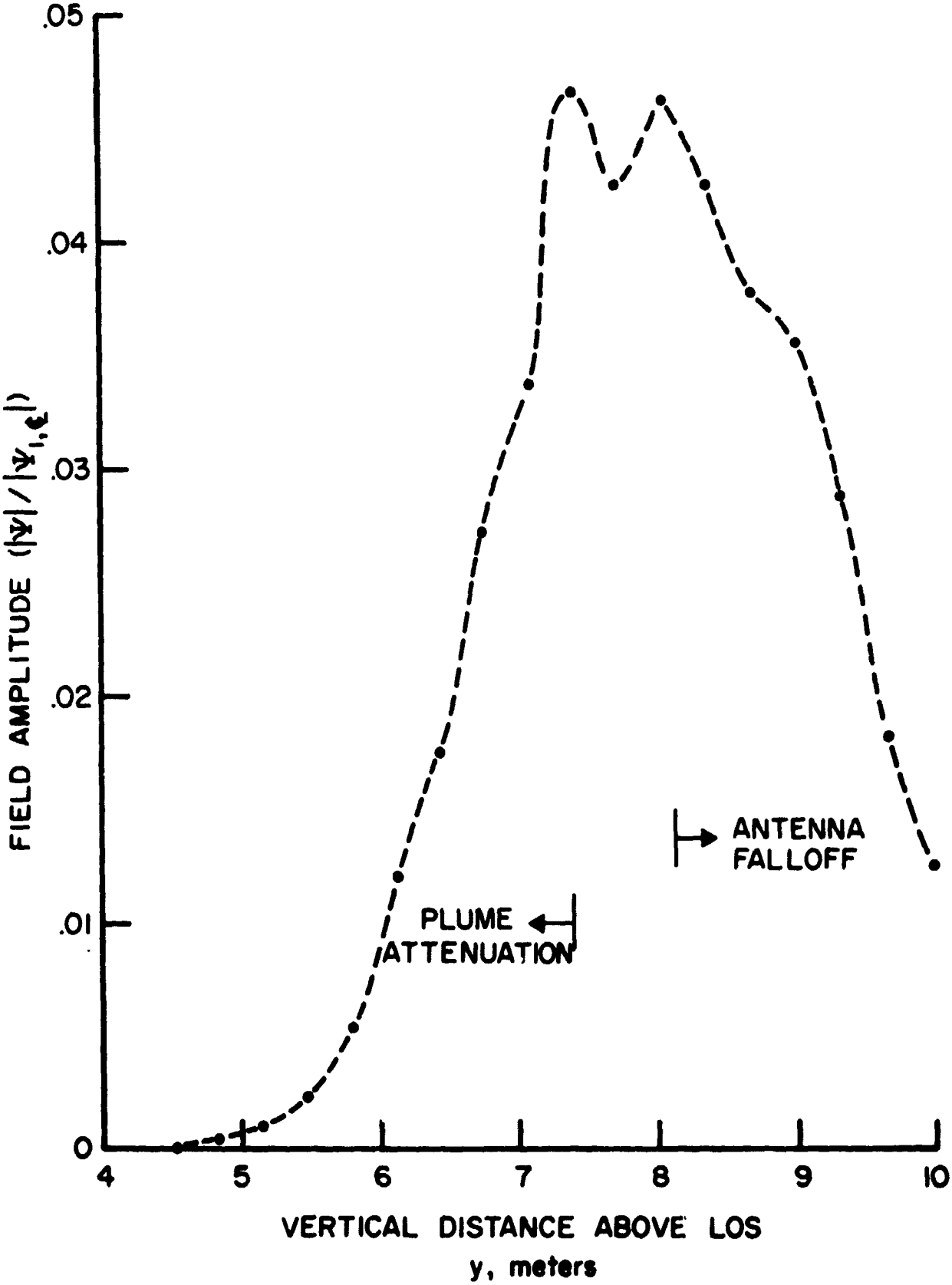

Figure 20. Normalized field amplitude vs. vertical distance just after passing the plume.

in time, then diffraction would produce a greater signal level at the transmitter location. The effect would be more noticeable at S-band than at the Range Safety frequency both because the mean plume is sharper-edged at low frequency and because the value of the diffraction parameter V (defined in Section 3) is greater, making the result more sensitive to details of the diffracting edge.

We can easily evaluate the expected attenuation if the plume edge were sharp. The angle at which the attenuated signal is half the peak value is 6.6°, and the values of a and b are 68 meters and 2.22 meters at this station. The diffraction parameter V is 4.1, and the expected ratio of the signal level at this value of V compared to that at the edge is

$$\frac{1}{2}(\pi V)^{-2} + 6 \text{ db} = -19 \text{ db}$$

The antenna pattern adds another -5 db so that the total result is -24 db; this value lies within the range of the measured data, and is not far from the result obtained when the plume has settled down to a steady state. The actual attenuation level should be calculated as an average over the fluctuating positions of the edge, and would be a little higher or lower than what we estimate here.

We had hoped to introduce simulated turbulence effects into these calculations in a manner similar to the way in which we treated the flight calculations. In the flight case we found little difference between turbulent and nonturbulent results. It now appears that our earlier results were strongly affected by numerical errors in the calculations under flight conditions, and that the effects of simulated turbulence could be significantly greater than those calculations indicate. Because we have attempted to improve the accuracy of the computational procedure under flight conditions, we were unable (within the available funds) to apply our turbulence model to the ground tests.

It is also worth noting that if our speculation that turbulence effectively sharpens the plume edge is correct, an accurate calculation applied to a mean flow field will tend to produce conservative (high) attenuation levels in the deeply shadowed region.

5.0 REVISIONS TO COMPUTATIONAL PROCEDURES

In Section 3 we showed that the computational procedure used in our earlier work to evaluate SRM plume attenuation in flight is inaccurate (overly conservative) for the deeply shadowed region. Performing an accurate calculation using FFT's requires large arrays, whose manipulation could result in very substantially greater computational costs. We have spent some time examining procedures which might be applied on a smaller computational grid, so that the entire calculation can be contained within the rapid-access memory of a typical large computer.

An alternative procedure to the full FFT-based computation which can be attractive when rapid-access storage is limited to use the FFT procedure on a small grid, but to supplement it by a semi-analytical procedure when the FFT solution fails to pass the accuracy test. Here we would approximate the behavior of the wave amplitude $\psi_{Z_0}(x',y')$ between mesh points by some convenient analytic function and calculate the contributions to the field amplitude $\psi_{Z_1}(x,y)$ by summing (coherently) the integrals of this function times the propagation kernel over the regions around each mesh point on the plane $Z = Z_0$. This procedure is expected to be much more time-consuming than an FFT solution for the same number of grid points, since it scales as NN' where N' is the number of points at which the convolution is evaluated by summation.

A procedure which leads to a relatively easily formulated algorithm is to assume that the logarithm of the field amplitude varies quadratically with position on the plane $Z = Z_0$. Discontinuities in magnitude, phase, and slope of ψ are minimal and an analytical expression for the contribution of the region near a mesh point in the plane $Z = Z_0$ to the amplitude at $Z = Z_1$ is easily obtained in terms of complex error functions.

In one dimension we represent the amplitude at $Z = Z_1$ as

$$\psi_{Z_1}(x_j) = \sqrt{\frac{1}{\lambda\Delta Z}} \sum_i \int_{x'_{i-\frac{1}{2}}}^{x'_{i+\frac{1}{2}}} \psi_{Z_0}(x')\, e^{-ik_0(x_j-x')^2/2\Delta Z}\, dx'$$

where $x'_{i\pm\frac{1}{2}} = \frac{1}{2}(x'_i + x'_{i\pm1})$. We approximate $\psi_{Z_0}(x')$ between mesh points x'_{i-1} and x'_{i+1} as

$$\psi_{Z_0} \approx \left\{\exp\ -(ax'^2 + bx' + c) + \frac{ik_0}{2\Delta Z}(x' - x_j)^2\right\}$$

where a, b, and c are complex coefficients which depend on x_j but not on x'. Then

$$ax'^2 + bx' + c = -\log \psi_{Z_0} + \frac{ik_0}{2\Delta Z}(x' - x_j)^2 = F(x')$$

These coefficients can be determined from the values of F at the mesh points x'_{i-1}, x'_i, and x'_{i+1} by solving the set of complex linear equations

$$ax'^2_{i-1} + bx'_{i-1} + c = F_{i-1}$$
$$ax'^2_i + bx'_i + c = F_i$$
$$ax'^2_{i+1} + bx'_{i+1} + c = F_{i+1}$$

With this approximation we have

$$\psi_{Z_1}(x_j) = \sqrt{\frac{1}{\lambda\Delta Z}} \sum_i G_{ij}$$

where

$$G_{ij} = \int_{x'_{i-\frac{1}{2}}}^{x'_{i+\frac{1}{2}}} \exp\left\{-(ax'^2 + bx' + c)\right\} dx'$$

To evaluate this we take

$$ax'^2 + bx' + c = (\alpha x' + \beta)^2 + R$$

where completing the square gives

$$\alpha = a^{\frac{1}{2}}$$

$$\beta = b/(2\alpha)$$

$$R = (4ac - b^2)/(4a)$$

Thus

$$G_{ij} = \int_{x'_{i-\frac{1}{2}}}^{x'_{i+\frac{1}{2}}} \exp\left\{-(\alpha x' + \beta)^2\right\} dx' \cdot \exp\left\{\frac{b^2 - 4ac}{-4a}\right\}$$

The substitution $\xi = \alpha x' + \beta$, $d\xi = \alpha\, dx'$ then leads to

$$G_{ij} = \frac{1}{\alpha} \int_{\xi_{i-\frac{1}{2}}}^{\xi_{i+\frac{1}{2}}} \exp\left\{-\xi^2\right\} d\xi \cdot \exp\left\{-\frac{b^2 - 4ac}{4a}\right\}$$

The integral is a line integral in the complex plane; by Cauchy's theorem it is independent of path since $e^{-\xi^2}$ is analytic. It can be expressed in terms of the error function of complex argument

$$\mathrm{erf}(Z) = \frac{2}{\sqrt{\pi}} \int_0^Z e^{-t^2}\, dt \quad , \qquad Z = x+iy$$

as

$$G_{ij} = \frac{\sqrt{\pi}}{2\alpha} \exp\left\{-\frac{b^2 - 4ac}{4a}\right\}\left[\mathrm{erf}(\xi_{i+\frac{1}{2}}) - \mathrm{erf}(\xi_{i-\frac{1}{2}})\right]$$

A subroutine which can be used tc evaluate the complex error function is included in the CERN* Computer Center Program Library. The routine CWERF (Kölbig, 1970; Gautschi, 1970) evaluates the function

$$w(Z) = e^{-Z^2}\left\{1 + \frac{2i}{\sqrt{\pi}} \int_0^Z e^{t^2}\, dt\right\}$$

which is related to the error function as

$$w(Z) = e^{-Z^2}\left[1 - \mathrm{erf}(-iZ)\right]$$

We have tested this algorithm for several simple problems. In each case we evaluate a reference solution by employing the FFT procedure on a closely spaced grid, and compare these results to those of the analytic solution evaluated on a series of coarser grids. The test problem is diffraction about a "fuzzy" edge:

$$|\psi_{Z_0}| = 1 \qquad x' > x_0$$

$$|\psi_{Z_0}| = \exp\left\{-(x' - x_0)^2/2A^2\right\} \qquad x' < x_0$$

with A and x_0 related such that $\psi_{Z_0}(x' = 0) = 0.5$.

Figures 21 through 27 show some results of these test calculations. In all cases the distances a and b are 40 and 260 meters and the frequency is 416 MHz. The diffracted results are expressed in terms of the angle ϕ, where $\phi = 0$ identifies $|\psi| = \frac{1}{2}|\psi_{max}|$ on the initial surface (effective edge position).

*Centre European pour Recherche Nucleaire

In Figure 21 we show the initial variation of amplitudes with position and the diffracted result (intensity vs. angle) for $A = 3.0$. Here the solution is evaluated using FFT's with 512 grid points. Figure 22 shows the same quantities for a 64-point calculation using the semi-analytic procedure. In each case the initial wave form is tapered at the right-hand side to reduce aliasing in the FFT solution. Figure 21 shows that the FFT results are still influenced by aliasing at scattering angles below about -20°. At greater values of ψ the low-resolution semi-analytic results agree within 5 to 10 db with the high-resolution FFT results; the agreement is better the larger ϕ, and can also be improved by going to a 128-point semi-analytic calculation. For our purposes the agreement with 64 points appears acceptable.

Figure 23 and 24 show the results of calculations with $A = 3.0$. Here the comparison can be extended to -30°, where the two calculations are within 10 db of each other. At 15° they are within 3 db. Part of the discrepancy here may be due to the low-resolution calculation's not being able fully to resolve the tail region. A 128-point calculation is within 3 to 4 db of the high-resolution results at 30° (Figure 25).

Figures 26 and 27 show results for a straightedge ($A = 0$). The low-resolution semi-analytic calculation is within 3 to 4 db of the average high-resolution FFT results at all angles. A comparable 64-point FFT solution (see Figure 10) would have been grossly in error at angles below -5 to -10°.

Scattering angles of interest for the Space Shuttle plume at high altitude are of the order 15°, and compare at constant V to about 22° in these calculations (because of the larger effective value of the distance a). It appears that the semi-analytic procedure developed here should be capable of giving satisfactory results for the Shuttle in flight. However, flight calculations require a two-dimensional computation.

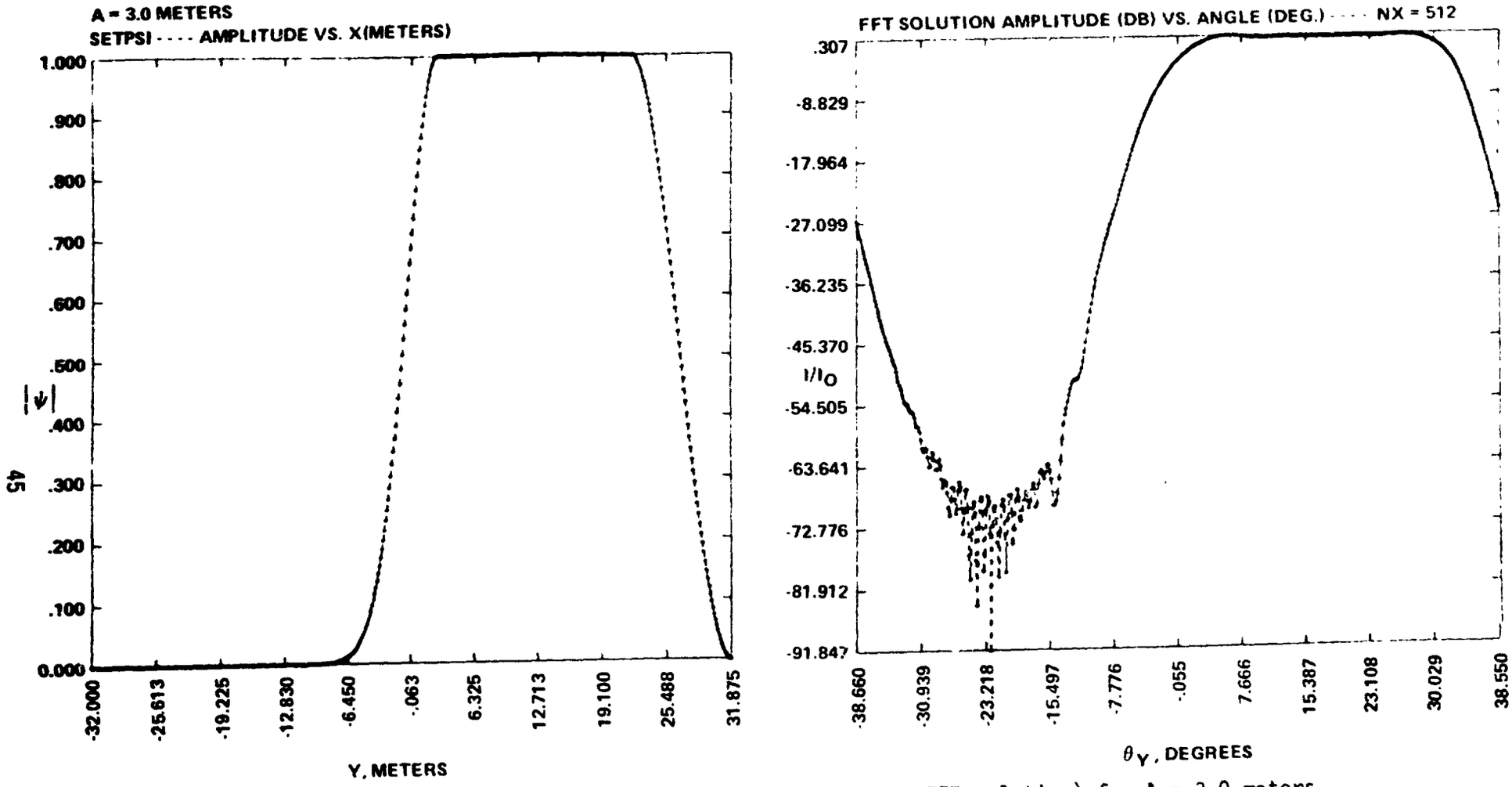

Figure 21. Diffraction about a "fuzzy" edge (512-point FFT solution) for A = 3.0 meters. Left, initial field amplitude vs. y. Right, diffracted intensity in db vs. θ_y (aliased at left).

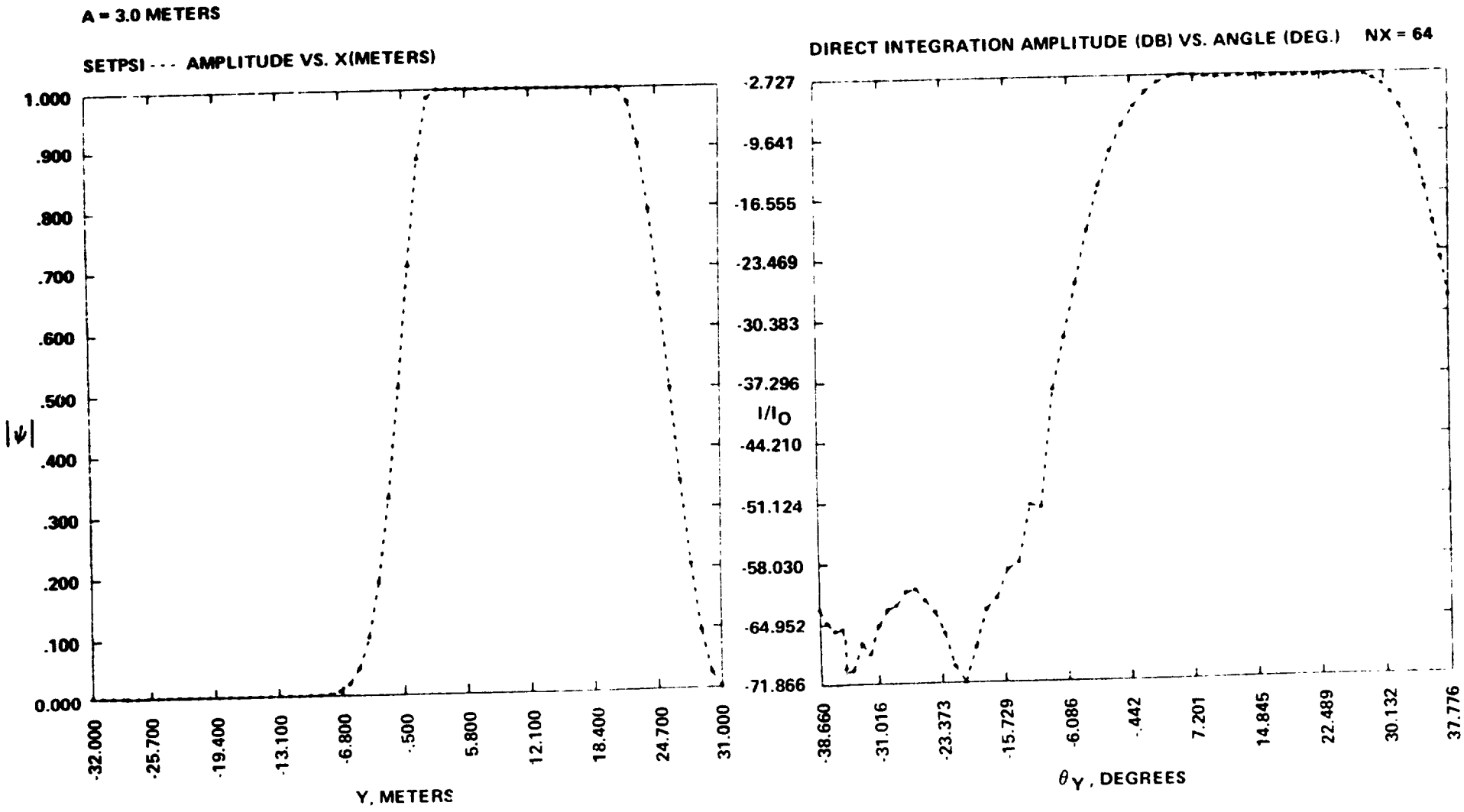

Figure 22. Diffraction about a "fuzzy" edge (64-point semianalytic solution) for A = 3.0 meters. Left, initial field amplitude vs. y. Right, diffracted intensity in db vs. θ_y.

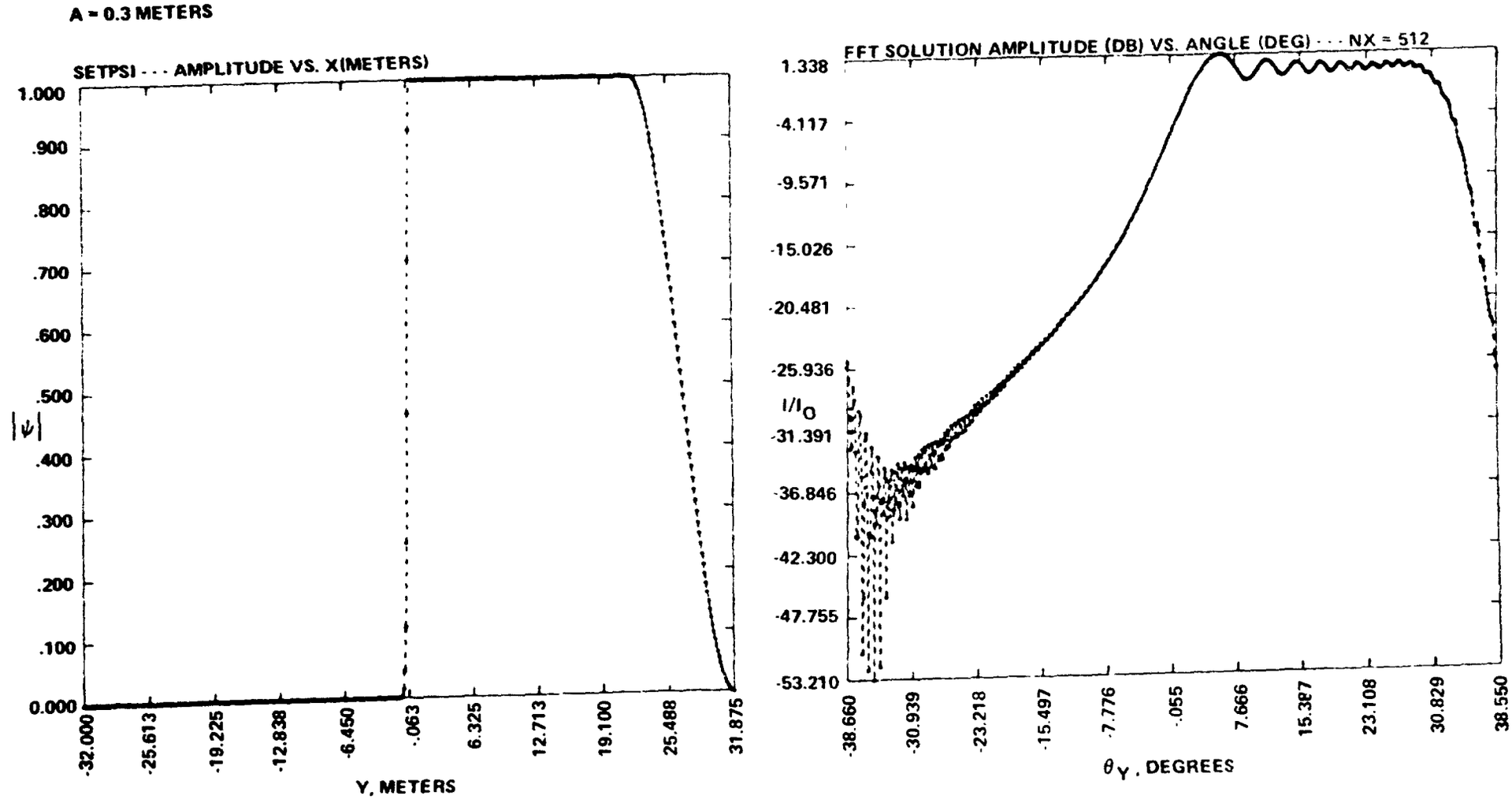

Figure 23. Diffraction about a "fuzzy" edge (512-point FFT solution) for A = 0.3 meters. Left, initial field amplitude vs. y. Right, diffracted intensity in db vs. θ_y (aliased at left).

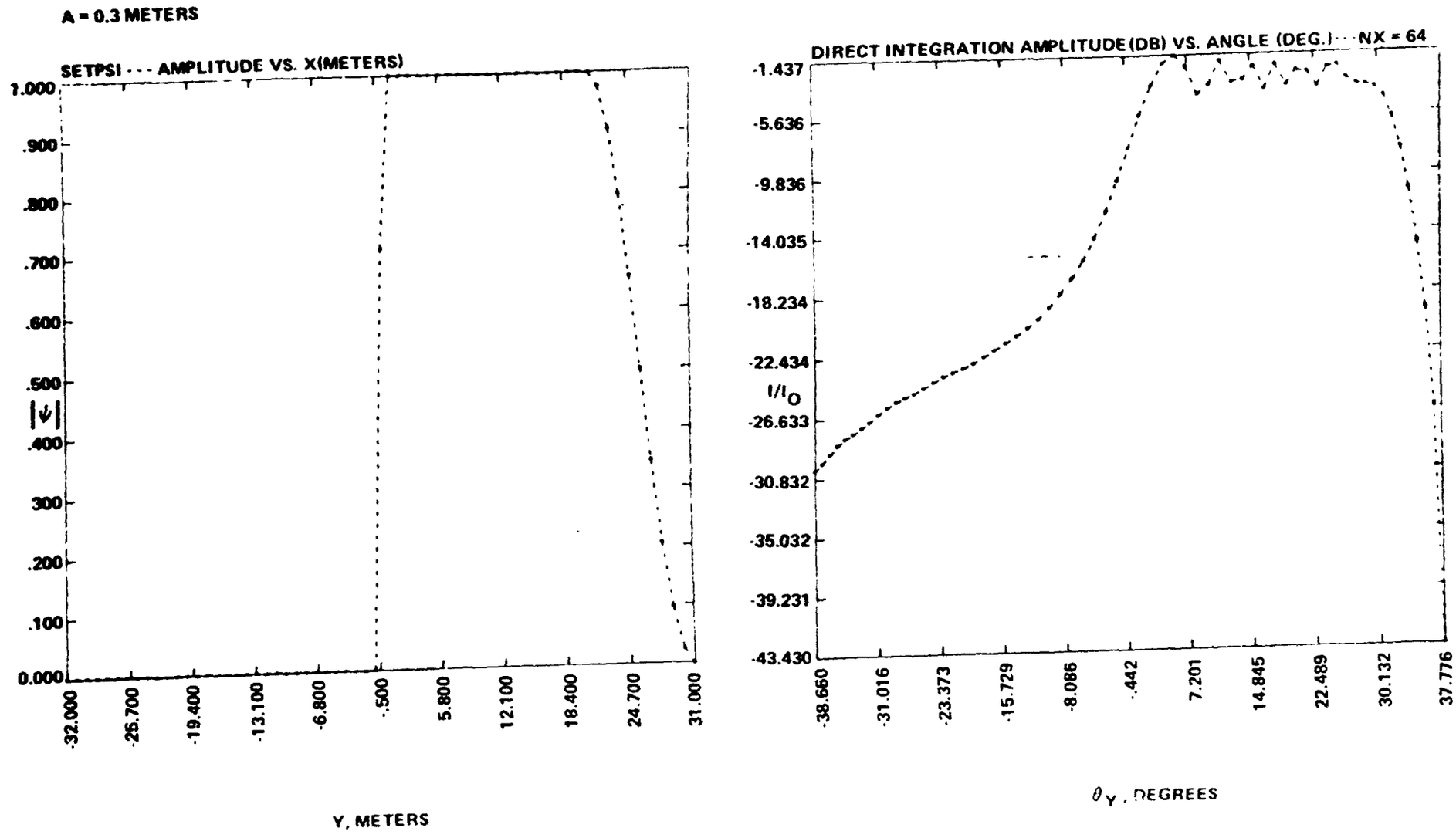

Figure 24. Diffraction about a "fuzzy" edge (64-point semianalytic solution) for A = 0.3 meters. Left, initial field amplitude vs. y. Right, diffracted intensity in db vs. θ_y.

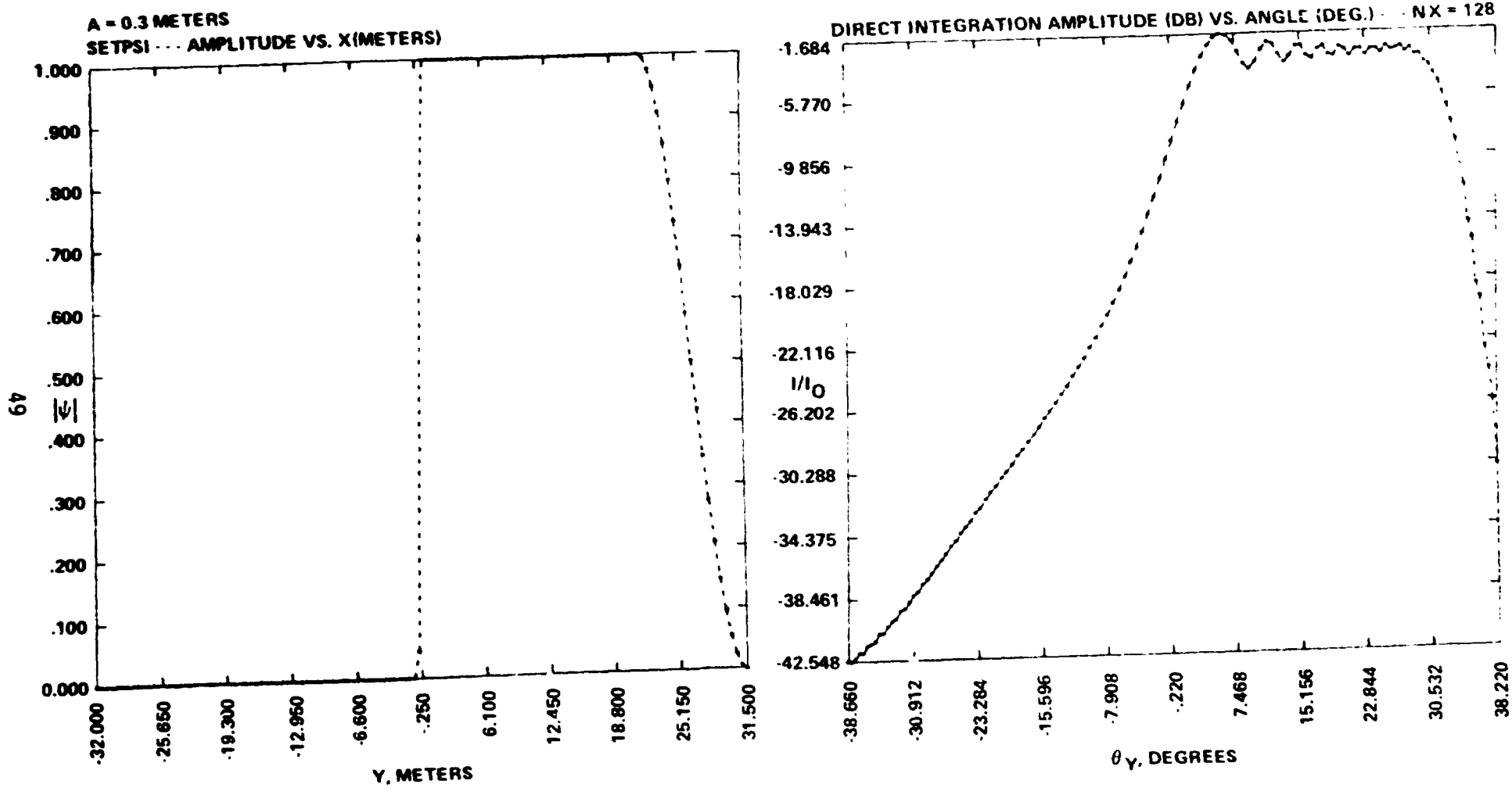

Figure 25. Diffraction about a "fuzzy" edge (128-point semianalytic solution) for A = 0.3 meters. Left, initial field amplitude vs. y. Right, diffracted intensity in db vs. θ_y.

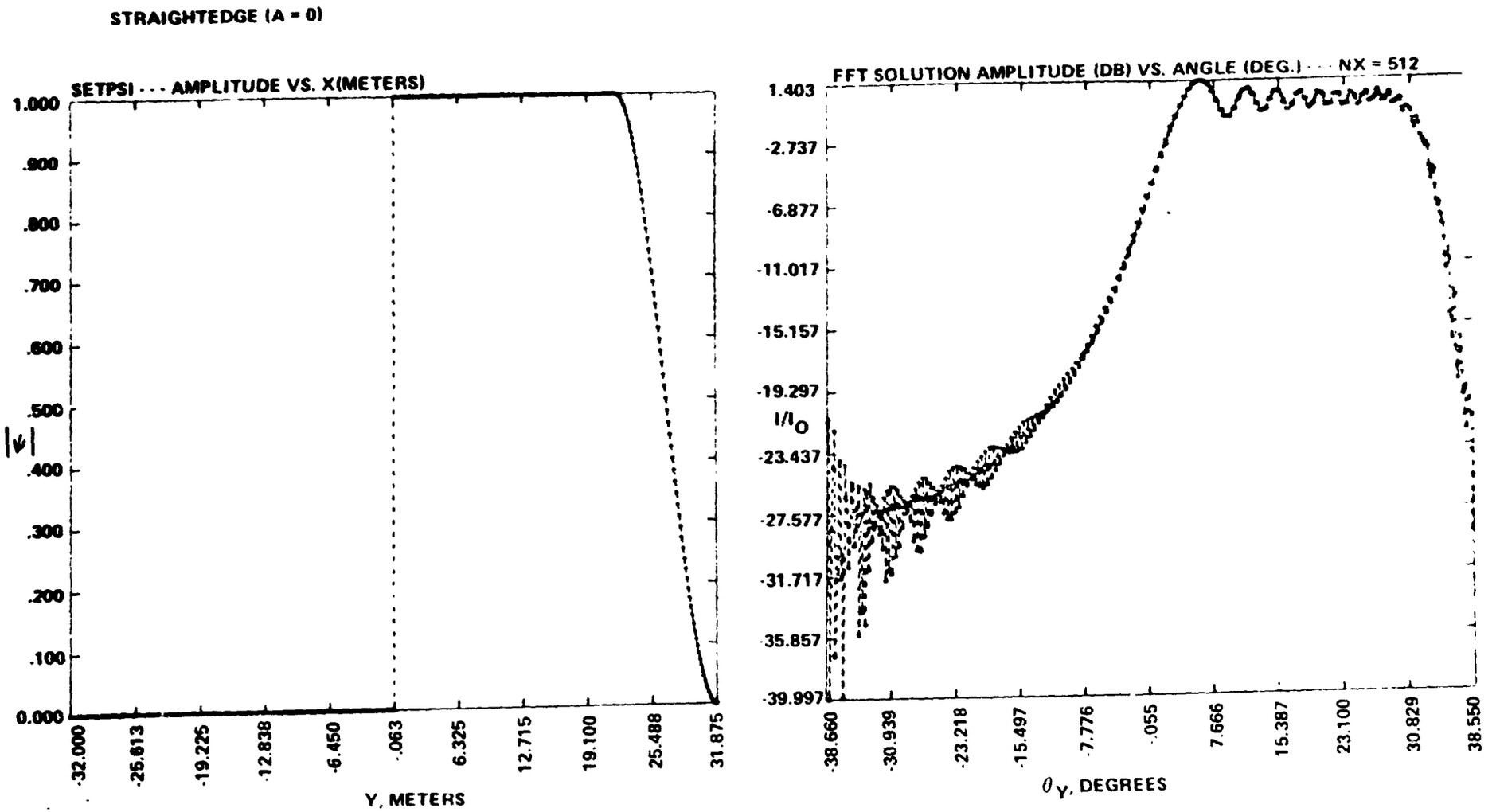

Figure 26. Diffraction about a straightedge (512-point FFT solution). Left, initial field amplitude vs. y. Right, diffracted field intensity in db vs. θ_y.

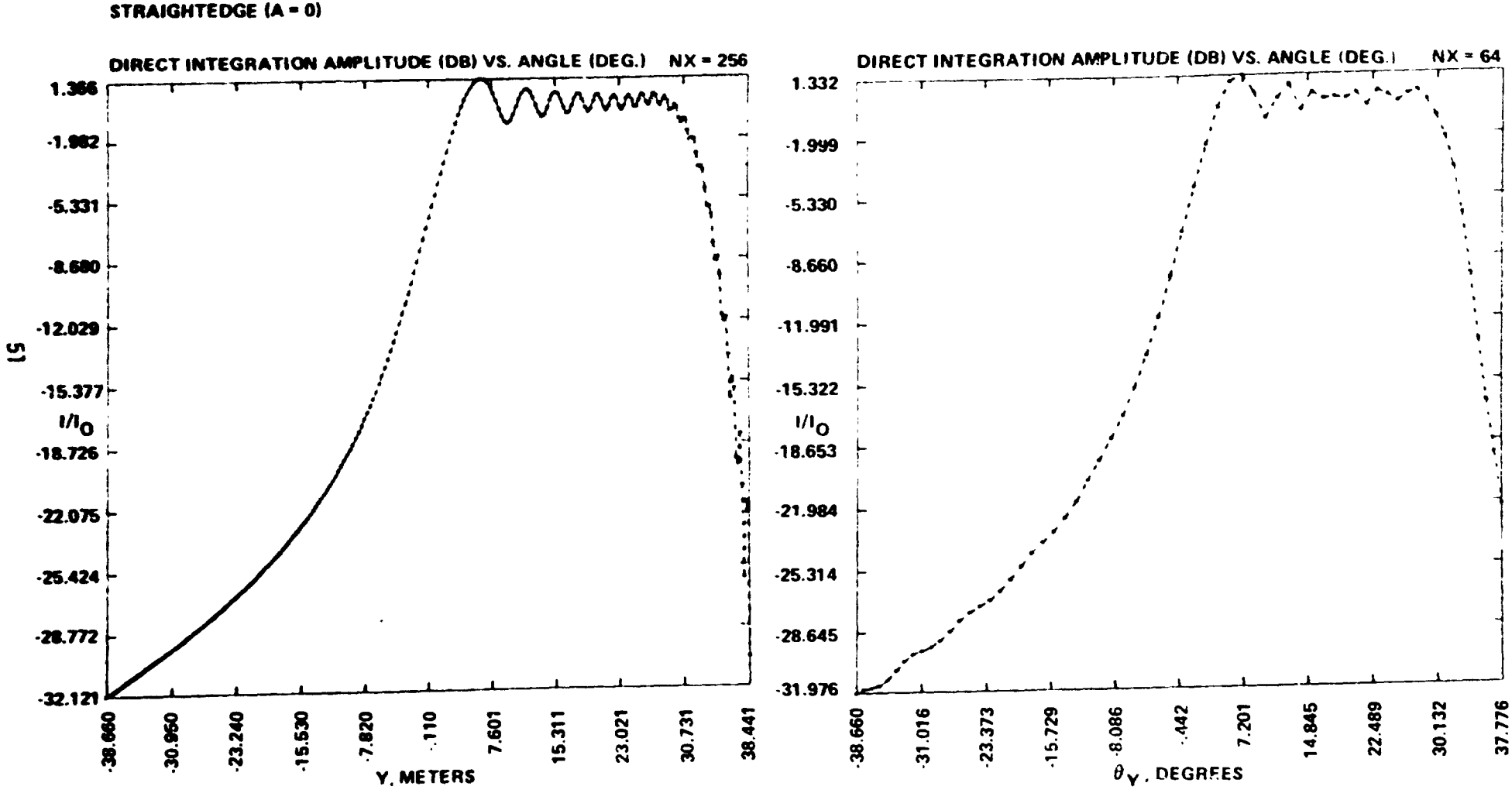

Figure 27. Diffraction about a straightedge. Comparisons of 256-point (left) and 64-point (right) semianalytic solutions.

The extension of this algorithm to two dimensions (x,y) is relatively straightforward. Here we write

$$\psi_{Z_1}(x_m, y_n) = \frac{1}{\lambda\Delta Z} \int_{x'_{i-\frac{1}{2}}}^{x'_{i+\frac{1}{2}}} \int_{y'_{j-\frac{1}{2}}}^{y'_{j+\frac{1}{2}}} \psi_{Z_o}(x',y') \, e^{-\frac{ik_o}{2\Delta Z}\left[(x'-x_m)^2 + (y'-y_m)^2\right]} \, dx' \, dy'$$

with $x'_{i\pm\frac{1}{2}} = \frac{1}{2}(x'_i + x'_{i\pm1})$ and $y'_{j\pm\frac{1}{2}} = \frac{1}{2}(y'_j + y'_{j\pm1})$. We approximate ψ in the vicinity of a mesh point (x'_i, y'_j) as

$$\psi_{Z_o} = \exp\left\{-(ax'^2 + bx' + c + dy' + ey'^2) + \frac{ik_o}{2\Delta Z}\left[(x'-x_m)^2 + (y'-y_m)^2\right]\right\}$$

so that

$$ax'^2 + bx' + c + dy' + ey'^2 = -\log \psi_{Z_o} + \frac{ik_o}{2\Delta Z}\left[(x-x_m)^2 + (y-y_n)^2\right]$$

$$= F_{ij}$$

The coefficients are now determined by a set of five linear complex equations

$$ax'^2_{i-1} + bx'_{i-1} + c + dy'_j + ey'^2_j = F_{i-1,j}$$

$$ax'^2_i + bx'_i + c + dy_j + ey'^2_j = F_{i,j}$$

$$ax'^2_{i+1} + bx'_{i+1} + c + dy'_j + ey'^2_j = F_{i+1,j}$$

$$ax'^2_i + bx'_i + c + dy'_{j-1} + ey'^2_{j-1} = F_{i,j-1}$$

$$ax'^2_i + bx'_i + c + dy'_{j+1} + ey'_{j-1} + F_{i,j+1}$$

Thus, we have

$$\psi_{Z_1}(x_m, y_n) = \frac{1}{\lambda \Delta Z} \sum_i \sum_j G_{ij,mn}$$

with

$$G_{ij,mn} = \int_{x'_{i-\frac{1}{2}}}^{x'_{i+\frac{1}{2}}} \exp\left\{-(ax'^2 + bx')\right\} dx' \cdot \int_{y'_{j-\frac{1}{2}}}^{y'_{j+\frac{1}{2}}} \exp\left\{-(ey'^2 + dy')\right\} dy' \cdot e^C$$

As before, we find

$$G_{ij,mn} = \frac{\pi}{4\alpha\gamma} \exp\left\{-\left[\frac{b^2}{4a} + \frac{d^2}{4e} - c\right]\right\}\left[\operatorname{erf}(\xi_{i+\frac{1}{2}}) - \operatorname{erf}(\xi_{i-\frac{1}{2}})\right] \times \left[\operatorname{erf}(\eta_{j+\frac{1}{2}}) - \operatorname{erf}(\eta_{j-\frac{1}{2}})\right]$$

where

$$\alpha = a^{\frac{1}{2}}$$
$$\gamma = e^{\frac{1}{2}}$$
$$\xi = \alpha x' + \beta$$
$$\eta = \gamma y' + \delta$$
$$\beta = b/2\alpha$$
$$\delta = d/2\gamma$$

Numerical difficulties can arise in applications of the above procedure unless care is exercised. One problem which we have encountered involves a large positive real part of either C or ξ^2 (or η^2), which can cause the CEXP routine to fail. In all cases the combination $C + \xi^2$ (or $C + \eta^2$) has a small real part, so that simply adding the exponents before performing the exponential operation,

rather than multiplying the exponentials, avoids this difficulty.

A more subtle problem is associated with the symmetry properties of the function $w(z)$ defined above, and the way the CWERF subroutine uses them in evaluating $w(z)$ for z not in the first quadrant. The relevant properties are

$$0 \le |w(x + iy)| \le 1 \qquad x,y > 0$$

$$w(-x + iy) = w^*(x + iy)$$

$$w(x - iy) = 2e^{y^2 - x^2}[\cos 2xy + i \sin 2xy] - w^*(x + iy)$$

Problems occur for z near the negative imaginary axis, since the real part of the exponential is large. The exponential comes from the term involving 1 in the definition of $w(z)$; because it is e^{-z^2}, it should cancel when multiplied by e^{z^2} in evaluating

$$\int_0^z e^{t^2}\,dt = \left[e^{z^2} w(z) - 1\right] \frac{\sqrt{\pi}}{2i}$$

Because of roundoff errors arising when one combines exponents to eliminate the first problem, cancellation is not perfect. One is left with a small difference between large numbers and the answer can be wildly in error.

This difficulty can be avoided by recognizing that the integral over a mesh region is independent of the sign of the square root chosen when calculating $\alpha = \sqrt{a}$. Thus it is sufficient to set $\alpha = -\alpha$ whenever using the principal part $(-\pi/2 < \arg \alpha \le \pi/2)$ of results in z's near the negative imaginary axis ($y < 0$ and $y^2 > x^2$). This results in β going to $-\beta$ and $z = \alpha x + \beta$ going to $-z$; the variable z now lies near the positive imaginary axis where $w(z)$ is bounded. The answer is unchanged, but difficulties

arising from the computer's carrying limited number of decimal places are eliminated.

6.0 REVISED PLUME INTERFERENCE CALCULATIONS FOR SPACE SHUTTLE

We have applied the computational procedure developed in the preceding section to evaluating the Range Safety signal attenuation by the SRM exhaust plume at an altitude of 37.5 km. This is the case which was found in our earlier work to have the broadest and deepest attenuation pattern.

The propagation of the signal through the exhaust plume was evaluated using the usual multiple-screen representation with FFT's. Because the diffraction parameter is large (due to the small distance b in Figure 7) near the plume centerline, large errors are expected for the signal amplitude incident upon any phase screen after the first. However, these large errors in ψ occur in regions where the attenuation is also very large, so that the signal amplitude emergent from that screen is in any case very small. This region has a negligible effect upon the value of ψ incident upon the next phase screen.

Once past the plume (or more appropriately, past the region of the plume for which we have flow field data) the signal is propagated to the far-field plane, again using FFT's. The signal amplitude on the next-to-last phase screen (this is the last screen for the exhaust plume) is stored for future use. In the "Talanov" coordinate system appropriate to the propagation step between the last plume station and the far-field plane, in which the signal would be a plane wave in the absence of the plume, we evaluate a contour line on the last plume station along which the plume-induced attenuation is 6 db. This contour defines the position of an effective plume edge for the propagation to the far-field plane. This contour is projected on the far-field plane (a simple translation, since the mesh has the same size on both planes in the transformed coordinate system), and each point within that contour is tested to see whether the Fresnel-zone accuracy criterion is obeyed.

We evaluate the shortest distance r_{min} from each point within the 6-db contour to that contour, and equate the distance S

in Figure 7 to r_{min}. We then ask whether the Fresnel zone width

$$\Delta x_{ZONE} = (\lambda Z'/2\, r_{min})$$

is greater or less than twice the mesh spacing δx (in these calculations $\delta y = \delta x$). Here Z' is the transformed propagation distance

$$Z' = \frac{Z_f\, Z}{Z_f + Z} = \frac{ab}{a + b}$$

If $\Delta x_{ZONE} > 2\ \delta x$, then we consider the FFT calculation to be sufficiently accurate, and the result for ψ on the far-field plane is left unchanged. If $\Delta x_{ZONE} < 2\ \delta x$, then our accuracy criterion has been violated, and we recalculate ψ using the semi-analyti direct integration procedure and the stored values of ψ' from the last plume station.

We have applied this procedure both to the relatively smooth mean flow field given by the LMSC/HREC calculation of plume properties and to a sharp-edged plume derived from that same calculation. (Recall that a possible explanation for the discrepancy between our calculations for the Thiokol experiments and the measured attenuation is that the plume is actually sharper-edged, as the result of instantaneous gradient steepening by turbulent distortions, than the mean flow.) The position of the sharp edge is arbitrarily defined as the 6-db contour on a phase screen just beyond the point of tangency of the plume-skimming ray. These results are compared in Figures 28 and 29, where we plot the far-field intensity ratio I/I_0 in db as a function of the angles θ_x and θ_y, respectively. (The antenna is on the side of negative θ_x and θ_y.) Both calculations show much less attenuation near tail aspect than does the full FFT calculation (Figure 5) given in our previous report. The sharp-edged plume produces much less attenuation near tail aspect than does the mean

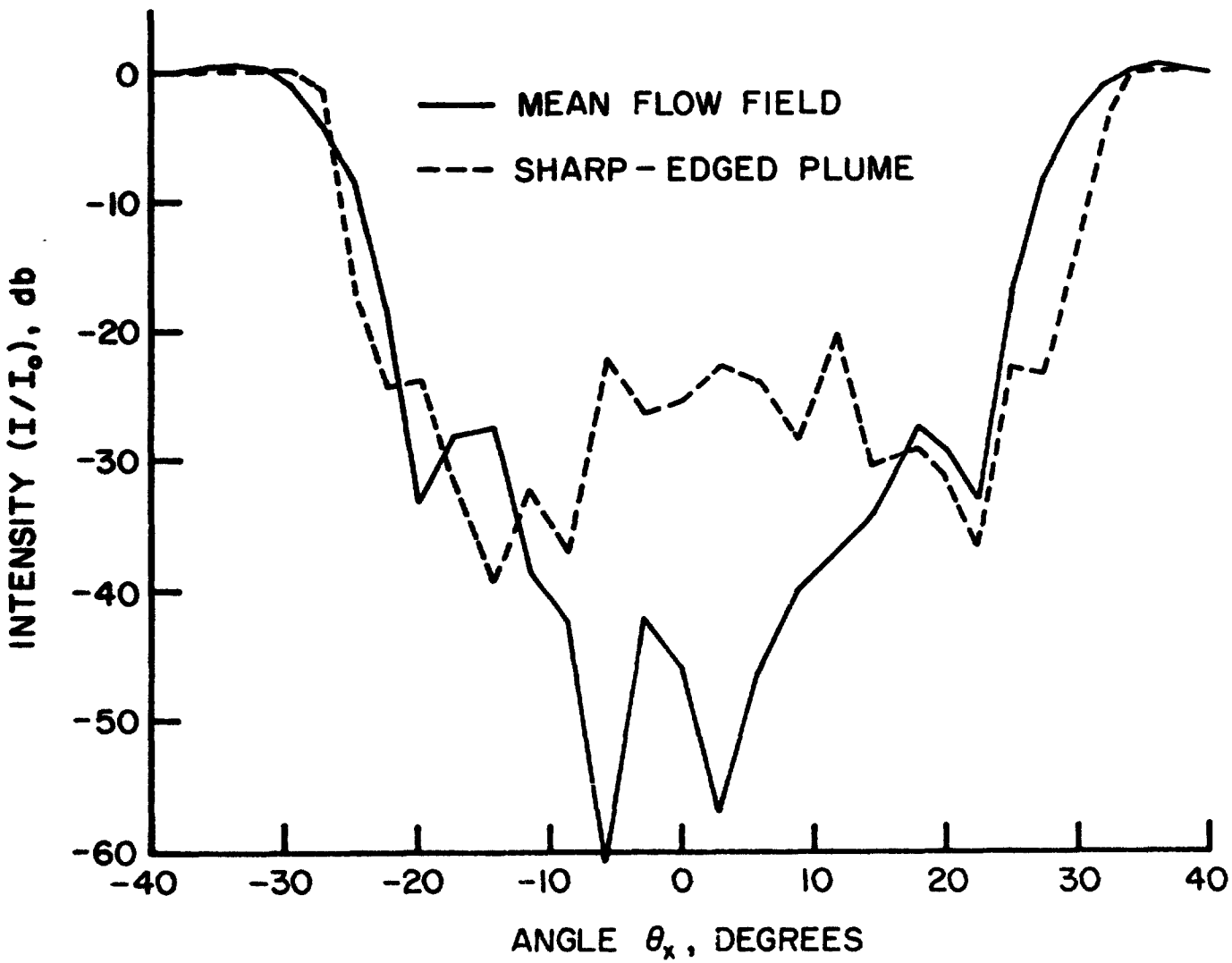

Figure 28. Calculations of Range Safety signal interference by Space Shuttle SRM plumes at 37.5 km altitude using the procedure of Section 5: Relative signal intensity I/I_o vs. aspect angle θ_x (in motor plane).

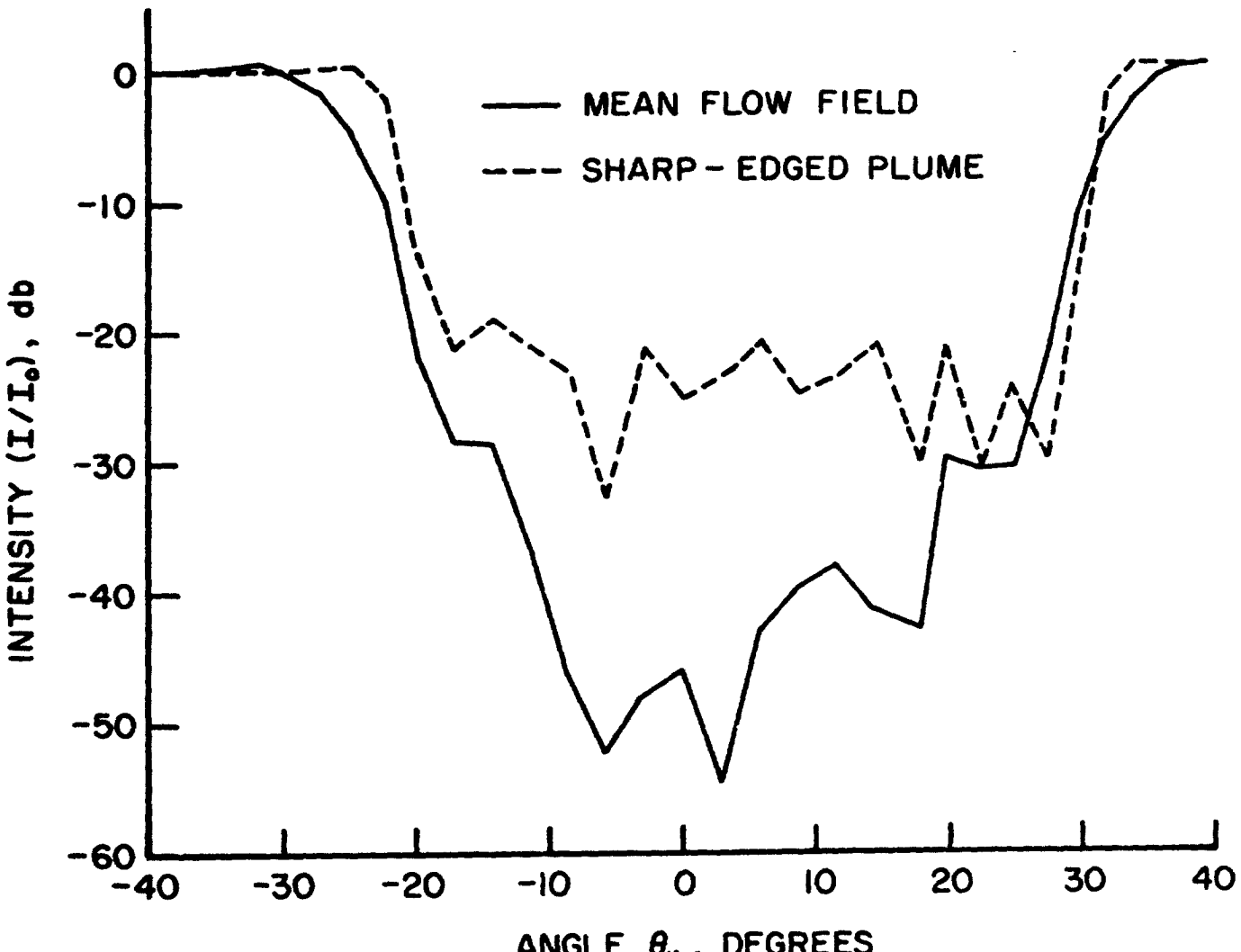

Figure 29. Calculations of Range Safety signal interference by Space Shuttle SRM plumes at 37.5 km altitude using the procedure of Section 5: Relative signal intensity I/I_0 vs. aspect angle θ_y (normal to motor plane).

flow field. In a rough sense, these two calculations can be regarded as upper and lower bounds to the expected signal strength; each propagation calculation is expected to be accurate, and the uncertainties are those associated with defining an instantaneous flow field.

Both calculations indicate that attenuations of the order of 30-35 db can occur at angles between 10 and 20°. These "holes" in the signal level pattern are deep enough to make the Range Safety system marginally operable if they actually occur in flight. The qualitative conclusion of our previous report that the Shuttle Range Safety signal could be adversely affected by the SRM exhaust plume still appears valid.

ACKNOWLEDGMENT

We thank J. Alex Thomson for several highly beneficial discussions concerning the accuracy of the propagation calculations and procedures for improving them. We also thank Keith Webb of Thiokol and Robert Martin of NASA (GFSC) for several helpful discussions of the SRM ground tests, S.D. Smith of Lockheed (HREC) for furnishing the exhaust plume flow field data used in this study, and Era N. Mann of NASA (MSFC) for her assistance and coordination throughout this study.

REFERENCES

Boynton, F.P., A.R. Davies, P.S. Rajasekhar, and J.A. Thomson (1977a), "Range Safety Signal Propagation through the SRM Exhaust Plume of the Space Shuttle", Physical Dynamics, Inc., Report PD-B-77-141.

Boynton, F.P., A.R. Davies, P.S. Rajasekhar, and J.A. Thomson (1977b), "Effects of Large, Absorbing Rocket Exhaust Plumes on RF Signals", JANNAF 10th Plume Technology Meeting, CPIA Publication 291, pp. 143-173.

Boynton, F.P., A.R. Davies, P.S. Rajasekhar, and J.A.L. Thomson (1977c), "FRENL: A Code to Calculate RF Attenuation by Rocket Exhaust Plumes", Physical Dynamics, Inc., Report PD-B-77-163.

Dash, S.M., and H.S. Pergament (1977), "The Analysis of Low Altitude Rocket and Aircraft Plume Flowfields: Modelling Requirements and Procedures", JANNAF 10th Plume Technology Meeting, CPIA Publication 291, pp. 53-131.

Gautschi, H.J. (1970), "Efficient Computation of the Complex Error Function" SIAM J. Numer. Analysis 7, p. 187.

Kalil, F. (1977), "Shuttle Solid Rocket Booster (SRB) Plume Attenuation Test Results, DM-1", NASA Goddard Space Flight Center X-862-77-280.

Kölbig, K.S. (1970), "Certification of Algorithm 363, Complex Error Function", CERN/DD/CO/70/13.

Poehler, H.A. (1969), "Rocket Exhaust Signal Attenuation and Degradation, Final Report", Pan American World Airways, Aerospace Services Division, Report ETR-TR-69-4.

Talanov, V.I. (1970), J. Exp. Theor. Phys. Letters 11, p. 799.

Vicente, F.A., E.C. Taylor, and R.W. Phelps (1967), "Analysis of Flame Effects on Measured Electromagnetic Propagation Data", J. Spacecraft 4, pp. 1069-1075.